A Simple Numerical Model of Calcium Spark Formation and Detection in Cardiac Myocytes

Gregory D. Smith,* Joel E. Keizer,# Michael D. Stern,§ W. Jonathan Lederer,¶ and Heping Cheng§

*Mathematical Research Branch, National Institutes of Health, Bethesda, Maryland 20814; #Institute for Theoretical Dynamics and Section on Neurobiology, Physiology, and Behavior, University of California, Davis, California 95616; §Laboratory of Cardiovascular Science, Gerontology Research Center, National Institutes of Health, Baltimore, Maryland 21224; and ¶Department of Molecular Biology and Biophysics, University of Maryland, Baltimore, Maryland 21201 USA

ABSTRACT The elementary events of excitation-contraction coupling in heart muscle are Ca^{2+} sparks, which arise from one or more ryanodine receptors in the sarcoplasmic reticulum (SR). Here a simple numerical model is constructed to explore Ca^{2+} spark formation, detection, and interpretation in cardiac myocytes. This model includes Ca^{2+} release, cytosolic diffusion, resequestration by SR Ca^{2+}-ATPases, and the association and dissociation of Ca^{2+} with endogenous Ca^{2+}-binding sites and a diffusible indicator dye (fluo-3). Simulations in a homogeneous, isotropic cytosol reproduce the brightness and the time course of a typical cardiac Ca^{2+} spark, but underestimate its spatial size ($\sim$1.1 μm vs. $\sim$2.0 μm). Back-calculating $[Ca^{2+}]_i$ by assuming equilibrium with indicator fails to provide a good estimate of the free Ca^{2+} concentration even when using blur-free fluorescence data. A parameter sensitivity study reveals that the mobility, kinetics, and concentration of the indicator are essential determinants of the shape of Ca^{2+} sparks, whereas the stationary buffers and pumps are less influential. Using a geometrically more complex version of the model, we show that the asymmetric shape of Ca^{2+} sparks is better explained by anisotropic diffusion of Ca^{2+} ions and indicator dye rather than by subsarcomeric inhomogeneities of the Ca^{2+} buffer and transport system. In addition, we examine the contribution of off-center confocal sampling to the variance of spark statistics.

INTRODUCTION

The recent discovery of "Ca^{2+} sparks" in cardiac myocytes via confocal microfluorimetry (Cheng et al., 1993) has greatly advanced our understanding of the subcellular events responsible for Ca^{2+} release from the sarcoplasmic reticulum (SR). The Ca^{2+} spark has been identified as an "elementary" Ca^{2+} release event under physiological conditions and may arise from the opening of a single SR Ca^{2+} release channel/ryanodine receptor (RyR) or a small number of such channels acting in concert (Cheng et al., 1993; Cannell et al., 1995; López-López et al., 1995; see also Lipp and Niggli, 1996; for a review see Cheng et al., 1996b). During cardiac excitation-contraction coupling, the stochastic recruitment of Ca^{2+} sparks by L-type Ca^{2+} channels in the sarcolemmal (SL) membrane is controlled by the mechanism of Ca^{2+}-induced Ca^{2+} release (CICR) (Fabiato, 1985). Summation of Ca^{2+} sparks gives rise to the global $[Ca^{2+}]_i$ transient, which activates the contractile myofilaments. Although there are important differences, localized intracellular Ca^{2+} release events similar to cardiac Ca^{2+} sparks have been observed in skeletal (Tsugorka et al., 1995; Klein et al., 1996) and smooth muscle (Nelson et al., 1995) that express different isoforms of the ryanodine receptor and have different ultrastructural organization of the cells. Furthermore, local Ca^{2+} elevations, dubbed "Ca^{2+} puffs" and "Ca^{2+} blips," have been observed in *Xenopus* oocytes (Yao et al., 1995; Parker and Yao, 1996) containing the inositol trisphosphate receptor, the second major branch of the intracellular Ca^{2+} release channel superfamily (Berridge, 1993).

Theoretically, the formation of a Ca^{2+} spark can be viewed as a reaction-diffusion problem involving Ca^{2+} release from the SR, cytosolic Ca^{2+} diffusion, reaction of Ca^{2+} with various Ca^{2+}-binding proteins (endogenous Ca^{2+} "buffers"), and re-sequestration of Ca^{2+} into the SR via ATP-dependent transport. The Ca^{2+}-indicator dye itself is a molecular species capable of binding Ca^{2+} and affecting its transport. The effect of both exogenous and endogenous Ca^{2+} buffers is complicated by the fact that these species may be mobile and thus capable of diffusing in both free and bound forms (Harkins et al., 1993; Roberts, 1993; Wagner and Keizer, 1994). Analysis of Ca^{2+} sparks further requires a theoretical framework by which one can infer the physiologically relevant free Ca^{2+} elevation from the experimentally measured signal, the indicator fluorescence. Initial observations and calculations suggested that the SR Ca^{2+} efflux during a Ca^{2+} spark is of the order of 3 pA (Cheng et al., 1993; Blatter et al., 1997), that the decay rate is dominated by diffusion (Cheng et al., 1995; Gómez et al., 1996), and that the rate of Ca^{2+} transport into the SR can influence the time-course of the Ca^{2+} spark (Gómez et al., 1996). However, because of the many fluxes involved in Ca^{2+} spark formation and other experimental and theoretical issues related to their detection (see Methods), quantitative modeling is warranted for understanding various mechanisms of Ca^{2+} spark formation and needed to correctly interpret data from fluorescence measurement.

Received for publication 2 October 1997 and in final form 8 April 1998.

Address reprint requests to Dr. Heping Cheng, Laboratory of Cardiovascular Science, Gerontology Research Center, NIA, NIH, 5600 Nathan Shock Drive, Baltimore, MD 21224. Tel.: (410) 558-8634; Fax: (410) 558-8150; E-mail: chengp@grc.nia.nih.gov.

0006-3495/98/07/15/18 $2.00

Many authors have contributed to the theoretical framework within which these calculations of Ca^{2+} sparks are performed (Neher, 1986; Stern, 1992a; Allbritton et al., 1992; Wagner and Keizer, 1994; Cannell et al., 1995). Preliminary calculations of Ca^{2+} puffs similar to those presented here were performed in an analysis of the validity of the rapid buffering approximation near a Ca^{2+} source (Smith et al., 1996). These calculations included a crude coarse-graining or averaging meant to simulate the optical blurring inherent in confocal microscopic measurements, but used parameters that were more relevant to *Xenopus* oocytes than cardiac myocytes. Analytical work based on the rapid buffering approximation provides an upper bound on the source strength required to produce a given elevated Ca^{2+}-bound indicator dye profile (Smith, 1996). Most recently, Pratusevich and Balke (1996) presented simulations of Ca^{2+} sparks to explore the effect of photon noise and out-of-focus events on the fidelity of the Ca^{2+} spark measurements. Several other studies have focused on Ca^{2+} binding to membrane phospholipids as well as electrodiffusion of Ca^{2+} within the diadic space that couples RyR's to the L-type channels (Langer and Peskoff, 1996; Soeller and Cannell, 1997).

Here we extend our preliminary work on the modeling of Ca^{2+} transport during localized Ca^{2+} elevations (Cheng et al., 1993; 1995; Gómez et al., 1996; Smith, 1996; Smith et al., 1996) and present a simple numerical model of spark formation and detection. Specifically, our goal is to understand what cellular features determine the size, amplitude, and kinetics of a Ca^{2+} spark and how the spatiotemporal properties of the fluorescence signals observed in confocal imaging are related to the space-time dynamics of the underlying $[Ca^{2+}]_i$ signal. To make the models more useful, we investigate the limits of the experimental work by exploring how the measurement of Ca^{2+} sparks perturbs the underlying free Ca^{2+} elevation. The inclusion of a realistic "point spread function" (PSF) into our calculations allows us to simulate the contribution of out-of-focus signal and to illustrate the effect of axial and radial off-center sampling of Ca^{2+} sparks. In addition, we present and discuss versions of the model that include anisotropy, subcellular inhomogeneities of Ca^{2+} handling mechanisms, and Ca^{2+} release from a spatially extended Ca^{2+} release site.

Description of model components and fluxes

The calculations of Ca^{2+} sparks presented here assume buffering reactions of the following form:

$$B_n + Ca^{2+} \underset{k_n^-}{\overset{k_n^+}{\leftrightarrow}} CaB_n \tag{1}$$

where n is an index over each buffer species; B_n represents a buffer binding site; and CaB_n represents Ca^{2+} bound to such a site. We assume a similar form for the reaction of cytosolic Ca^{2+} with the indicator dye fluo-3, which can exist in both Ca^{2+}-free (F) and Ca^{2+}-bound (CaF) forms. To incorporate the diffusion of Ca^{2+} and indicator dye in both forms, as well as immobilize Ca^{2+} through binding to stationary endogenous Ca^{2+} buffers, we solve a finite difference approximation to a set of reaction-diffusion equations of the following form (Stern, 1992a; Wagner and Keizer, 1994):

$$\frac{\partial[Ca^{2+}]}{\partial t} = D_C\nabla^2[Ca^{2+}] + J_{dye} + J_{buffers} + J_{pump} + J_{leak} + J_{ryr} \tag{2}$$

$$\frac{\partial[CaF]}{\partial t} = D_F\nabla^2[CaF] - J_{dye} \tag{3}$$

$$\frac{\partial[CaB_n]}{\partial t} = -J_n \tag{4}$$

where D_F and D_C are the diffusion coefficients for the indicator dye and free Ca^{2+} (all the endogenous buffers are assumed to be immobile; see below) and $J_{buffers}$ in Eq. 2 are given by $J_{buffers} = \Sigma_n J_n$. The various fluxes ($J_{dye}$, $J_{buffers}$, J_{pump}, J_{leak}, and J_{ryr}) are detailed below along with comments on our choice of parameter values (see Tables 1 and 2).

Flux due to Ca^{2+} release via the RyR (J_{ryr})

In most simulations presented here, we model Ca^{2+} release from the SR as originating at a virtual point source rather than an extended release site (Langer and Peskoff, 1996; Blatter et al., 1997); that is, $J_{ryr} = \sigma_{ryr}\delta(\vec{r})$, where σ_{ryr} is the time-dependent source strength (in micromoles per second) and $\delta(\vec{r})$, the Dirac delta function, is a sharply peaked function indicating the focal release of Ca^{2+} at the origin (Smith et al., 1996). The standard form of σ_{ryr} (see Table 1) is equivalent to a 10-ms pulse of 2 pA amplitude injected into an infinite medium; however, the simplicity of the model allows a range of source strengths and duration to be explored. Results were also obtained for Ca^{2+} release from extended sources (see Fig. 9 and related text).

The free Ca^{2+} diffusion coefficient

The diffusion coefficient for free Ca^{2+} (D_C) in aqueous solution of physiological ionic strength has been estimated to be 700–780 $\mu m^2/s$ (Wang, 1953). The value for diffusion of ions or uncharged molecules inside cytosol is usually reduced by a factor of 2–2.5, presumably due to tortuosity (i.e., obstacles force diffusion to follow a convoluted route) as well as increased viscosity. Values used in previous models range from 100 $\mu m^2/s$ (Langer and Peskoff, 1996) to 600 $\mu m^2/s$ (Pratusevich and Balke, 1996). We used a free Ca^{2+} diffusion coefficient of 250 $\mu m^2/s$ as our standard parameter value for D_C.

Fluxes due to Ca^{2+} indicator dye and endogenous stationary buffers (J_{dye} and $J_{buffers}$)

The fluxes for the indicator dye and each endogenous buffer take similar forms:

$$J_{dye} = -k_F^+[Ca^{2+}]([F]_T - [CaF]) + k_F^-[CaF] \quad (5)$$

$$J_n = -k_n^+[Ca^{2+}]([B_n]_T - [CaB_n]) + k_n^-[CaB_n] \quad (6)$$

In the first of these equations, $[F]_T$ is the total concentration of indicator dye, and k_F^+ and k_F^- are association and dissociation rate constants. Because we assume that the diffusion constant of the indicator dye is not affected by the binding of Ca^{2+}, and that the initial concentration profile of the indicator is uniform, the concentration profiles of Ca^{2+}-free indicator dye are given at all times by $[F] = [F]_T - [CaF]$ (Wagner and Keizer, 1994). Similarly, for each component of the sum that defines $J_{buffers}$, $[B_n]_T$ is the total concentration of buffer n; k_n^+ and k_n^- are association and dissociation rate constants; and the concentration of free buffer binding sites is taken to be $[B_n] = [B_n]_T - [CaB_n]$.

Endogenous Ca^{2+} buffer parameters. Table 2 summarizes our knowledge of endogenous Ca^{2+} buffers in cardiac myocytes on the basis of biochemical measurement (for a review see Bers, 1991) and functional studies (Sipido and Wier, 1991). Those buffers possessing specific Ca^{2+} binding sites include calmodulin and the contractile regulatory protein troponin C. Although they are less specific to Ca^{2+}, we include the phospholipid membranes of the sarcoplasmic reticulum (outer leaflet) and the sarcolemma (inner leaflet) as two additional Ca^{2+} buffers because the anion groups on the membrane surface constitute a low affinity, high capacity Ca^{2+} binding site (Bers et al., 1985; Post and Langer, 1992). These protein and membrane Ca^{2+} ligands were considered immobile in our model simulation.

Indicator dye (fluo-3) parameters. Though fluo-3 is unsuitable for two-wavelength ratiometric measurement of $[Ca^{2+}]_i$, it has been the indicator of choice for detecting Ca^{2+} sparks. Ca^{2+}-bound fluo-3 fluoresces ~200 times more intensely than its Ca^{2+}-free counterpart (Harkins et al., 1993). This high F_{max}/F_{min} ratio results in high signal contrast and high signal-to-noise ratio, accounting in part for its superiority (in the context of detecting local $[Ca^{2+}]_i$ elevations) over other widely used ratiometric Ca^{2+} indicators such as fura-2 and indo-1. In addition, the visible excitation wavelength (488 nm) of fluo-3 produces little autofluorescence and is expected to induce less photodamage in dye-loaded cells. Our Ca^{2+} spark model assumes that the fluorescence signal (in the absence of optical blurring) at a given spatial position is directly proportional to the local concentration of Ca^{2+}-bound indicator ([CaF]).

Fluo-3 is a penta-valent anion (mol wt 765) and is predicted to have a diffusion coefficient of 90 $\mu m^2/s$ (Wang, 1953; Harkins et al., 1993). However, the apparent diffusion coefficient of fluo-3 measured in skeletal muscle fibers ranges only between 12 to 30 $\mu m^2/s$ (Harkins et al., 1993), suggesting that 80% of the indicator (or equivalently, an individual dye molecule 80% of the time) is bound to immobile cellular constituents. Because of this and other experimental evidence that fluo-3 interacts with proteins of large molecular weight (e.g., aldolase; see Harkins et al., 1993), we have included fluo-3 immobilization in our model by either 1) partitioning the simulated indicator into two fractions, one stationary and one mobile, or 2) using a reduced, apparent diffusion coefficient for the indicator of 20 $\mu m^2/s$. We use the second method here, a decision justified because it reduces the number of parameters needed to characterize fluo-3, easing the interpretation of our calculations. However, it should be noted that the accuracy of this method depends on indicator dye and endogenous buffer parameters. For example, the Ca^{2+} profile predicted by the steady-state rapid buffering approximation is given by an equation in which the diffusion coefficient and concentration of mobile buffer occur as a product (see Eq. 10 in Smith, 1996, where $\varphi_j = D_j[B_j]_T K_j$). This implies that when buffer parameters are such that the rapid buffering approximation is valid, the simplified representation of fluo-3 transport is also accurate as time increases. However, given the moderate kinetics of fluo-3 used here, the validity of this approximation decreases in simulations that involve high concentrations of indicator dye (see Fig. 3).

Recent work indicates that the cytoplasmic environment also alters the interaction of the indicator with Ca^{2+}, markedly slowing both the dissociation rate [$k_F^- = 200$–$700\ s^{-1}$ in solution (Eberhard and Erne, 1989) versus $90\ s^{-1}$ inside skeletal muscle fiber (Harkins et al., 1993)] and the association rate [$k_F^+ = 80\ \mu M^{-1}s^{-1}$ in vivo (Harkins et al., 1993) versus $\sim 1000\ \mu M^{-1}s^{-1}$ in vitro (Eberhard and Erne, 1989)]. Because the k_F^+ and k_F^- are not equally affected, the dissociation constant (K_F) of fluo-3 for Ca^{2+} is increased from 0.4 μM to nearly 1–3 μM (Harkins et al., 1993). The exact cause for these changes is unclear. These effects were included in the model through our choice of reduced association ($k_F^+ = 80\ \mu M^{-1}s^{-1}$) and dissociation ($k_F^- = 90\ s^{-1}$) rates for fluo-3 in our reference parameter set (see Table 2). It should be noted that if the changes in the interaction of the dye with calcium in the cytoplasmic environment are due to the same binding that reduces the apparent diffusion coefficient of the dye, our assumption that the diffusion coefficient is independent of calcium binding may be violated. For simplicity, such effects were not considered here.

Flux due to Ca^{2+}-ATPases (J_{pump}) and passive leak (J_{leak})

Ca^{2+} resequestration by Ca^{2+} ATPases located in the SR membrane is a component of the model. The turnover rate as a function of instantaneous, local $[Ca^{2+}]_i$ is (Bassani et al., 1994)

$$J_{pump} = \frac{v_{pump}^{max}[Ca^{2+}]^m}{K_{pump}^m + [Ca^{2+}]^m}, \quad (7)$$

where K_{pump} is 184 nM, m is 3.98, and v_{pump}^{max} is 208 $\mu M s^{-1}$. The contribution of SL Na^+/Ca^{2+} exchanger is ignored

because of its minor role in regulating cellular $[Ca^{2+}]_i$ transients in rat ventricular myocytes (Balke et al., 1994). Because we do not explicitly keep track of the concentration of Ca^{2+} in the SR, the model requires an SR leak to balance J_{pump} when Ca^{2+} is at the background concentration (c_∞ = 0.1 μM). The magnitude of the SR leak is thus constant and given by

$$J_{leak} = -J_{pump}(c_\infty) = -\frac{V_{pump}^{max} c_\infty^m}{K_{pump}^m + c_\infty^m}. \quad (8)$$

Optical blurring: the point spread function

The light microscopic image of a dimensionless optical point, the so-called point spread function (PSF), extends in three dimensions and is elongated along the optical axial direction. Although confocal modality is designed to reduce axial as well as lateral blurring, a confocal image is never blur-free. Reported confocal PSFs have an axial full width at half-maximum (FWHM) of 0.7–1.4 μm and lateral FWHM of ~0.4 μm (e.g., Cheng et al., 1993; Pratusevich and Balke, 1996), comparable to the dimensions of a Ca^{2+} spark. Thus, we have taken optical blurring into account in these simulations. Our model PSF, $G(x, y, z)$, is a 3-D Gaussian function having axial ($FWHM_z$) and lateral ($FWHM_{xy}$) full width at half-maximum of 0.8 μm and 0.4 μm, respectively

$$G(x, y, z) = g(x, \sigma_{xy})g(y, \sigma_{xy})g(z, \sigma_z) \quad (9)$$

where $g(w, \sigma) = (2\pi\sigma)^{-1/2}\exp(-w^2/2\sigma)$ and σ_{xy} and σ_z are related to the FWHM in the axial and lateral directions through $g(\text{FWHM}/2) = g(0)/2$, that is, $\sigma_{xy} = (0.4\ \mu\text{m})^2/(8 \ln 2)$ and $\sigma_z = (0.8\ \mu\text{m})^2/(8 \ln 2)$. Thus, in our calculations, the value of simulated fluorescence at any given position is given by a numerical approximation to the convolution of the simulated dye profile with the model PSF given above

$$[\text{CaF}]_{avg}(x; Y_{offset}, Z_{offset}) = \int\int\int [\text{CaF}](x', y', z')G(x - x', Y_{offset} - y', Z_{offset} - z')dx'\,dy'\,dz' \quad (10)$$

where the integral is taken over the simulation volume. The parameters Y_{offset} and Z_{offset} represent the degree to which the origin of the spark is out of register with the center of the PSF, while x is the distance along the line scan. In this manuscript, simulation results are often reported as F/F_0, by which we mean $[\text{CaF}]_{avg}/[\text{CaF}]_\infty$, where $[\text{CaF}]_\infty$ is the resting fluorescence, i.e., the concentration of CaF when the dye is in equilibrium with the background Ca^{2+} concentration

$$[\text{CaF}]_\infty = \frac{c_\infty [F]_T}{K_F + c_\infty}. \quad (11)$$

Implementation of model

The finite difference scheme used to numerically solve Eqs. 2–8 is presented in the Appendix. In its simplest form, the model components (e.g., exogenous Ca^{2+} buffers, indicator dye, and SR Ca^{2+}-ATPases) are assumed to be homogeneously distributed in the cytosol, diffusion of mobile molecules is isotropic, and the Ca^{2+} release responsible for the Ca^{2+} spark defines the origin of a spherical polar coordinate system. Under these conditions, all concentration profiles are spherically symmetric throughout the simulation. Because of its simplicity and computational efficiency, spherical symmetry is assumed in many of the simulations presented here. However, even in these "radial" simulations, the model PSF is anisotropic, so calculations for optically blurred sparks off-center in the axial direction ($Z_{offset} > 0$, $Y_{offset} = 0$ in Eq. 10) are different from sparks off-center in the transverse direction ($Y_{offset} > 0$, $Z_{offset} = 0$).

Some anisotropies in Ca^{2+} sparks have been attributed to cellular structure and anisotropic diffusion (Cheng et al., 1996b; Parker et al., 1996) rather than imaging. To investigate the effects of inhomogeneously distributed Ca^{2+}-ATPases and Ca^{2+}-binding proteins, anisotropic diffusion of Ca^{2+} ions and indicator, and release from an extended source of Ca^{2+}, we have also implemented a simulation using a cylindrical (i.e., an axisymmetric) coordinate system, where r represents the distance from a Ca^{2+} release site in the transverse direction (parallel to the plane of a Z-line) and z represents the longitudinal distance (perpendicular to the plane of a Z-line) from the origin of the Ca^{2+} spark. The finite difference scheme described in the Appendix is a description of our numerical implementation of this model. The spherically symmetric simulation is easily derived from it.

In both the radial and cylindrical simulations, the initial condition for Ca^{2+} is a uniform background concentration ($[Ca^{2+}] = c_\infty = 0.1\ \mu$M). At the beginning of the simulation, endogenous Ca^{2+} buffers and exogenous indicator dye are in equilibrium with Ca^{2+}. These concentrations are also used in a Dirichlet (absorbing) boundary condition for each variable distant from the Ca^{2+} release site, that is, at $r = R_{max}$ and $z = Z_{max}$. Thus, in locations where the source has no effect, the solution is required to be in equilibrium with Ca^{2+} at all times (see p. 7, Morton and Mayers, 1994). In all calculations, R_{max} and Z_{max} are >10 μm, a value large enough that this choice does not influence the numerical results.

EXPERIMENTAL METHODS

Confocal immunofluorescence imaging

Single cells were prepared from rat hearts using a standard method (Cheng et al., 1993). After isolation, the cells were resuspended in normal extracellular saline solution and allowed to settle into a soft pellet. The cells were resuspended in −20°C ethanol to fix and permeabilize them and then processed for immunofluorescence (Kieval et al., 1992). The cells were exposed to a rabbit primary antibody to the SR Ca^{2+} ATPase and then treated with an FITC-labeled goat anti-rabbit antibody. We used a Zeiss LSM-410 microscope to image the immunolocalization of the SR Ca^{2+}

ATPase in the cells (see Fig. 6). The sarcomeric distribution of the enzyme was assumed to be proportional to the fluorescence intensity in the confocal section. The final distribution pattern was a signal-averaged image of the distribution around the *Z*-line.

Other experimental methods

Single ventricular myocytes were isolated from adult Sprague-Dawley rats (2–3 months old, weight 225–300 g) using standard enzymatic techniques, as reported previously (Xiao et al., 1997). Cells were loaded with the Ca^{2+} indicator by incubation with 10 μM Fluo-3 AM (Molecular Probes, Eugene, OR) for 12 min and then stored in HEPES buffer solution containing (in mM) 137 NaCl; 5.4 KCl; 1.2 $MgCl_2$; 1.2 NaH_2PO_4; 1 $CaCl_2$; 10 glucose and 20 Hepes (pH 7.4). Confocal imaging of spontaneous Ca^{2+} sparks was performed using a Zeiss LSM-410 inverted confocal microscope (Carl Zeiss, Inc., Germany) at a pixel width of 0.15 μm and a scan rate of 2.0 ms per line. The axial and radial resolutions of the imaging system were 0.9 and 0.4 μm, respectively. Image data were analyzed using IDL software (Research Systems, Boulder, CO). All experiments were conducted at room temperature (21–23°C).

RESULTS

Ca^{2+} flux underlying elementary Ca^{2+} release events

Fig. 1 *A* shows a space-time plot of a simulated "Ca^{2+} spark" produced by a 2 pA, 10 ms local Ca^{2+} release, as observed along a line placed 500 nm laterally from the release origin, with the PSF depicted in Eq. 9. For comparison, experimental data of an average Ca^{2+} spark from a rat ventricular myocyte are displayed in panel *B*. Sample traces of time courses and spatial profiles of the simulated spark are shown in panels *C* and *D*, respectively. When the simulated linescan was directly aligned with the spark center (not shown), normalized peak fluorescence, F/F_0, was as high as 3.76, similar to the brightest sparks seen in cells (Song et al., 1997; Blatter et al., 1997). As the scan line moved radially away from the center, the simulated peak

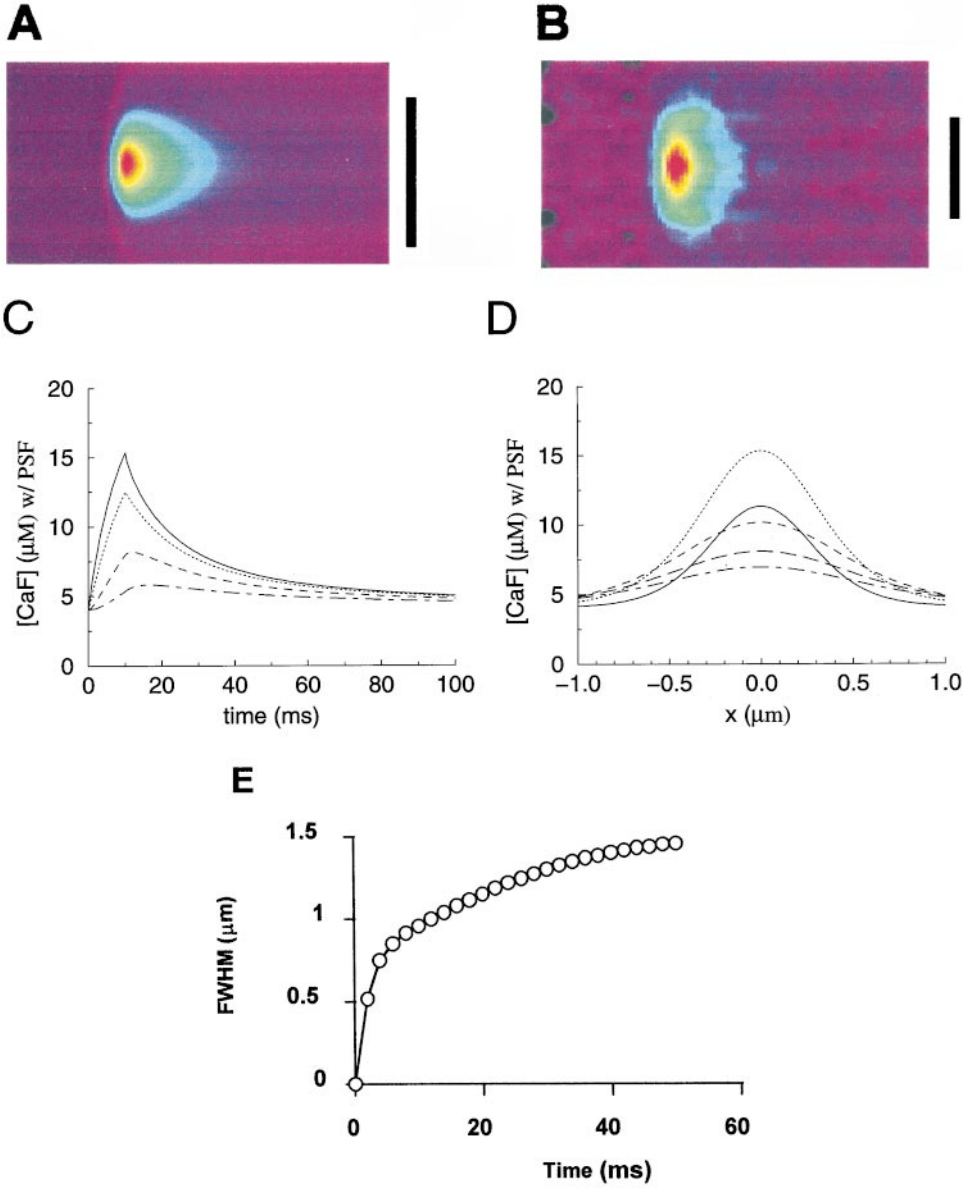

FIGURE 1 Properties of model Ca^{2+} spark. (*A*) Simulated and (*B*) experimental linescan image of Ca^{2+} sparks. To produce the image in panel *B*, 12 sparks from rat ventricular myocytes are aligned and averaged twice by adding their original images and their spatially reversed images. Scale bars: 2 μm. Time: 200 ms from left to right. (*C*) Simulated confocal spot recording of time courses of the model Ca^{2+} spark at different degrees of offset. From top to bottom, Y_{offset} = 0.0, 0.25, 0.5, and 0.75 μm; Z_{offset} is zero. (*D*) Fluorescence ([CaF]) profiles at five different times after the beginning of an in-focus (Y_{offset} = Z_{offset} = 0.0 μm) Ca^{2+} release event which occurs at t = 0. In ms: t = 5 (*solid line*), 10 (*dotted line*), 20 (*dashed line*), 30 (*long-dashed line*), and 40 (*dot-dashed line*). (*E*) Spark breadth (FWHM) as a function of time. For simulations in panels *A* and *E*, Y_{offset} = 0.5 μm and Z_{offset} = 0. All other parameters used are listed in Tables 1 and 2. After Ca^{2+} release terminates ($t > 10$ ms), the time course of the square of the FWHM gives an apparent diffusion coefficient for Ca^{2+} of 31 $\mu m^2/s$ (not shown).

amplitude was reduced while the time to peak was blunted and the decay time was increased (Fig. 1 *C*). At the representative distance shown (Y_{offset} = 0.5 μm), the peak F/F_0 was 2.01, the half decay time ($T_{1/2}^{decay}$) was 25.3 ms, and the FWHM was 0.89 μm at time of peak F/F_0 (t = 12 ms). Panels *D* and *E* show that the spread of the fluorescence in space exhibited two phases: a rapid initial expansion, rendering the flattened head of the comet-shaped spark in the linescan image (panels *A* and *B*), followed by a progressive growth that reached a FWHM of 1.40 μm at 30 ms after release was terminated (panel *E*).

Experimentally, the local increase of fluorescence of a Ca^{2+} spark is ~2.0 and the time constant of decay is around 20 ms (Fig. 1 *B*). The amplitude and rates of rise and decline of the simulated Ca^{2+} spark are thus comparable with the experimental data. However, the FWHM of the model spark is only half that observed experimentally (1.7–2.2 μm, Cheng et al., 1993; López-López et al., 1995; see below). Thus all the salient measures of Ca^{2+} sparks (with the exception of FWHM) can be readily reproduced by the radial model using a Ca^{2+} flux resembling unitary RyR current seen in lipid bilayer [~2 pA at 0 mV and 2.4 mM SR luminal Ca^{2+} (Tinker et al., 1993); 5.4–22.3 ms mean open time in the presence of ATP and 0.1 μM cytosolic Ca^{2+} and pCa 0.48–2.0 on the luminal side (Lukyanenko et al., 1996)]. This is consistent with the notion that Ca^{2+} sparks arise from single RyR channel openings; however, it is also compatible with the multiple-channel hypothesis of spark origin if the RyR in vivo has a reduced conductance or if RyR-RyR interaction is required to provide a longer effective mean open time (see below).

Physiological determinants of Ca^{2+} spark properties

Identifying cellular and molecular features involved in the shaping of Ca^{2+} spark properties is essential not only to understanding physiological modulation of elementary Ca^{2+} signaling, but also to integrating data in various tissues and species, and to devising strategies to experimentally manipulate SR Ca^{2+} release at the elementary level. To this end, model simulation can be exploited to gain insights that may not be easily obtained with experiment (e.g., dissecting contributions from each of the Ca^{2+} handling mechanisms). Starting from the standard parameter set described in Tables 1 and 2, we systematically varied model parameters (e.g., source strength and duration, the abundance of endogenous Ca^{2+} buffers, and the maximum rate of Ca^{2+} resequestration) over several orders of magnitude and studied subsequent changes in the properties of simulated Ca^{2+} sparks. Additional simulations with variable dye properties, spatial inhomogeneities, anisotropy, and spatially extended sources are deferred to later sections.

Spark brightness (peak F/F_o)

As expected, the amplitude or "brightness" of a simulated Ca^{2+} spark was very sensitive to the magnitude of the Ca^{2+}

TABLE 1 Model parameters

Parameter	Definition	Standard Value
	Local Ca^{2+} release from the SR	
i_{Ca}	Amplitude of elemental Ca^{2+} release	2 pA
F	Faraday's constant	96500 C/mol
Z	Valence of Ca^{2+} ion	2
	Diffusion of free Ca^{2+} and fluo-3	
D_C	Diffusion coefficient of free Ca^{2+} in cytosol	250 $\mu m^2/s$
D_F	Diffusion coefficient of fluo-3 and Ca^{2+}-fluo-3 in cytosol	20 $\mu m^2/s$
	fluo-3	
$[F]_T$	Total concentration of fluo-3 (see Table 2)	
k_F^+	Association rate constant for Ca^{2+} binding to fluo-3	
k_F^-	Dissociation rate constant of Ca^{2+} from fluo-3	
K_F	$= k_F^-/k_F^+$	
	Ca^{2+} resequestration by SR Ca^{2+}-ATPases	
v_{pump}^{max}	Maximum rate of Ca^{2+} reuptake	208 μM/s
K_{pump}	Michaelis constant	0.184 μM
m	Hill coefficient	3.9
	Ca^{2+} Buffering (see Table 2)	
$[B_n]_T$	Total concentration for each Ca^{2+} buffer	
k_n^+	Association rate constant for Ca^{2+} binding	
k_n^-	Dissociation rate constant of Ca^{2+} from ligand	
K_n	$= k_n^-/k_n^+$	
c_∞	Intracellular free Ca^{2+} concentration at rest	100 nM
	PSF of confocal microscope	
$FWHM_z$	Axial full width at half-maximum	0.8 μm (σ_z = 0.115 μm^2)
$FWHM_{xy}$	Lateral full width at half-maximum	0.4 μm (σ_{xy} = 0.0289 μm^2)

TABLE 2 Dye and endogenous Ca^{2+} buffers

Ca^{2+} Buffer	k_n^+ ($\mu M^{-1}s^{-1}$)	k_n^- (s^{-1})	$[B_n]_T$ (μM)	K_n (μM)
Fluo-3	80	90	50	1.13
Calmodulin	100	38	24	0.38
Troponin C	39	20	70	0.51
SR membrane	115	100	47	0.87
SL membrane	115	1000	1124	8.7

source (Fig. 2 *B*). For Ca^{2+} fluxes of 0.5–4.0 pA, peak F/F_0 varied nearly in proportion to the source strength (Fig. 2 *B*). Thus, under these conditions, the fluorescence signal is not saturated (see also Fig. 3 *E*), even though the local Ca^{2+} concentration (Stern, 1992a,b; Langer and Peskoff, 1996; Soeller and Cannell, 1997; see below) is expected to be much greater than the dissociation constant of fluo-3 (K_F = 1.13 μM). This occurs because the indicator and free Ca^{2+} are not at equilibrium during the spark event. Additionally, the minimal detection volume, or "voxel" ($\sim$0.13 μm^3) is larger than the microdomain of saturating Ca^{2+} (see below). Indeed, recent experimental data show that depletion of SR Ca^{2+} reduced spark amplitude (Satoh et al., 1997; Song et al., 1997) and that the reduced amplitude is linearly correlated with the caffeine-releasable SR Ca^{2+} load (Song et al., 1997). Thus, both theory and experiment reinforce the idea that changes in spark amplitude can result from changes in the underlying Ca^{2+} flux.

The intensity of the simulated fluorescence signal depends also on the release duration. Given a long-lasting Ca^{2+} flux of 2 pA, the local fluorescence signal did not reach its peak level until $\sim$50 ms elapsed (Fig. 2 *A*). It takes time both to "load" the endogenous Ca^{2+} buffer and for the dye to follow the free Ca^{2+} change. Hence, changes in the duration of Ca^{2+} release can alter spark amplitude. This result indicates that interpretation of optically measured spark amplitude is equivocal, in contrast with electrophysiological measurement of channel currents. Furthermore, this finding may also help to resolve a paradoxical observation that a skeletal muscle spark is $\sim$3 (Klein et al., 1996) or 5–10 times (based on "noise analysis" and in the presence of 10 mM exogenous mobile buffer, EGTA) (Tsugorka et al., 1995) smaller in amplitude than a cardiac spark, despite the fact that cardiac and skeletal RyR's are closely related isoforms. This calculation suggests that the difference might reside in a tissue-dependent open duration for in vivo gating of RyR.

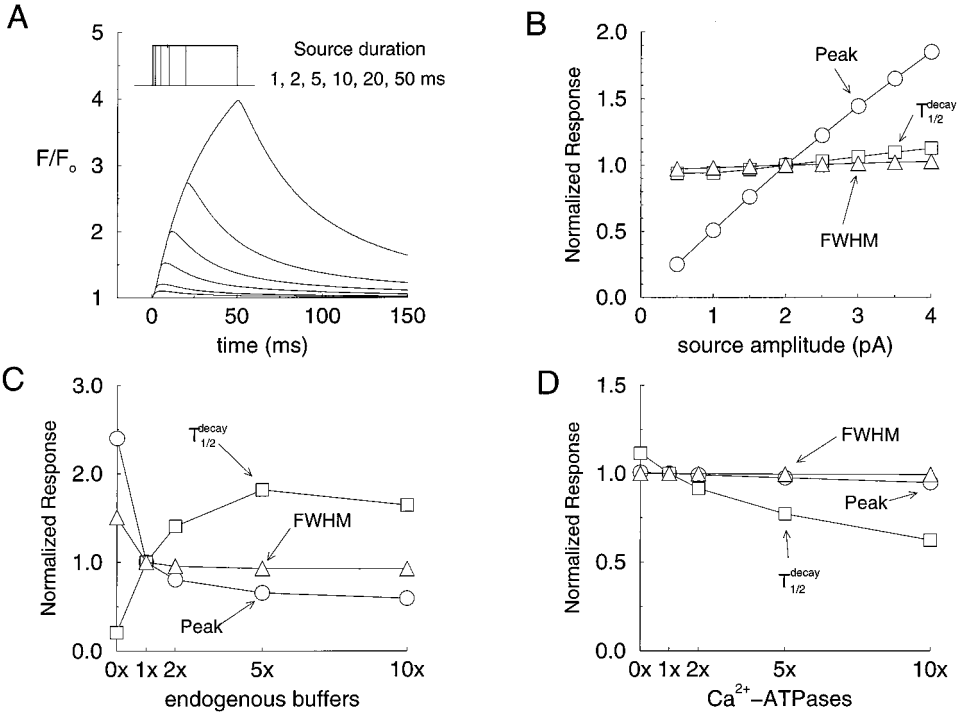

FIGURE 2 Parameter sensitivity study revealing the determinants of spark size, amplitude, and kinetics. (*A*) Duration of Ca^{2+} release. A family of time courses for the square pulse of 2 pA amplitude and duration of 1, 2, 5, 10, 20, or 50 ms are shown in the inset. Even at 50 ms the fluorescence signal has not reached the steady state. (*B*) Source amplitude is varied from 0.5 to 4.0 pA for a square pulse of 10 ms duration. The values of peak (*circles*), FWHM (*triangles*), and half-time of decay (*squares*) are plotted for each source strength, normalized to the value for our standard source strength, which was 2 pA. The numerical values for 2 pA are [CaF] = 8.20 μM at peak, a FWHM = 0.89 μm, and a half-time of decay of 25.3 ms. Note that sensitivity to the source amplitude is peak $\gg T_{1/2}^{decay} >$ FWHM. (*C*) Concentration of endogenous buffers is varied so that they are all either absent (0×) or at 1×, 2×, 5×, or 10× their standard concentrations (see Table 2). Normalized peak (*circles*), FWHM (*triangles*), and half-time of decay (*squares*) are plotted. (*D*) Maximum turnover rate of the SR Ca^{2+}-ATPases is varied, and normalized peak (*circles*), FWHM (*triangles*), and half-time of decay (*squares*) are plotted. SR pumps, even at 10 times their standard value, have little effect on peak or FWHM, and only a small effect on the half-time of decay. For all simulations, Y_{offset} = 0.5 μm, Z_{offset} = 0.

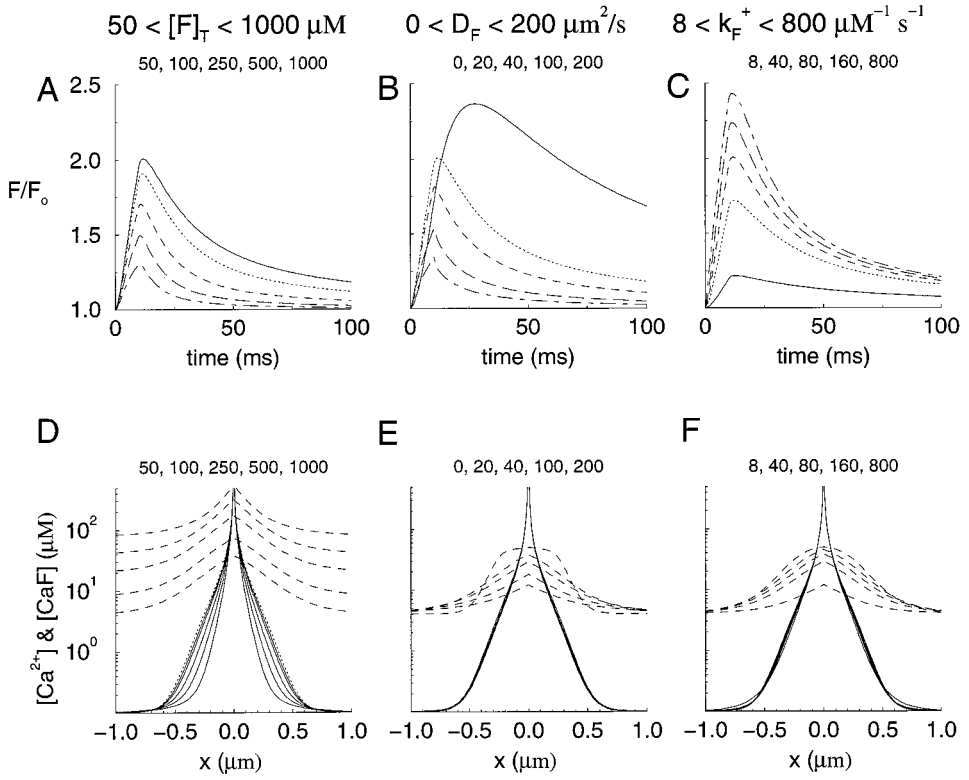

FIGURE 3 Effects of indicator dye parameters on spark properties. (*A–C*) Simulated time course of normalized, blurred fluorescence signal (F/F_0), with $Y_{offset} = 0.5$ μm and $Z_{offset} = 0$, and standard parameters (see Tables 1 and 2) unless otherwise noted. (*A*) Effect of variable amount of Ca^{2+} indicators. From top to bottom: total dye concentration ($[F]_T$) is 50, 100, 250, 500, and 1000 μM. Note that the F/F_0 is greater when there is less indicator, indicating that the indicator is perturbing the Ca^{2+} profile (see *panel D*). (*B*) Effect of varying the mobility of the dye. From top to bottom, D_F takes values of 0 (immobile), 20, 40, 100, and 200 $\mu m^2/s$. For stationary dye, note the marked differences in terms of amplitude, time to peak, and relaxation. (*C*) Effect of dye rate constants. From bottom to top, the Ca^{2+} association rate constant of the indicator is increased from 8 to 40, 80, 160, and 800 $\mu M^{-1}s^{-1}$ and the corresponding dissociation rate constants are 9, 45, 90, 180, and 900 s^{-1}, rendering K_F unchanged. (*D–F*) $[Ca^{2+}]$ (*solid line or dotted line*) and [CaF] (*dashed lines*) profiles at $t = 10$ ms. Parameters identical to panels *A–C*, respectively, except that $Y_{offset} = Z_{offset} = 0$. (*D*) Uppermost CaF profile (*dashed line*) and lowermost Ca^{2+} profile (*solid line*) are from simulation with total dye concentration ($[F]_T$) of 1000 μM. *Dotted line* shows the Ca^{2+} profile with no fluo-3. (*E*) Uppermost CaF profile (*dashed line*) and uppermost Ca^{2+} profile (*solid line*) are from simulation with immobile indicator ($D_F = 0$ $\mu m^2/s$). (*F*) Uppermost CaF profile (*dashed line*) and lowermost Ca^{2+} profile (*solid line*) are from simulation with fastest dye kinetics ($k_F^+ = 800$ $\mu M^{-1}s^{-1}$ and $k_F^- = 900$ s^{-1}).

Varying the amount of endogenous stationary Ca^{2+} buffer had a moderate effect on spark amplitude (Fig. 2 *C*). Peak F/F_0 decreased by ~30% in the presence of 10-fold more Ca^{2+} buffer and increased by 2.4-fold if all endogenous Ca^{2+} buffer was removed. This suggests that variations in intracellular Ca^{2+}-buffering capacity, as well as release flux and duration, may contribute to the difference in Ca^{2+} spark amplitudes across cell type. Interestingly, the SR Ca^{2+} ATPase, whether totally inactive or enhanced by an order of magnitude in our simulations, had virtually no effect on spark amplitude (Fig. 2 *D*). This is in good agreement with the recent observation that spark amplitude is unchanged when SR Ca^{2+} ATPase activity was either abolished by thapsigargin or stimulated via β-adrenergic-mediated signal transduction (Gómez et al., 1996).

Spark decay time ($T_{1/2}^{decay}$)

The half-time of decay, $T_{1/2}^{decay}$, for Ca^{2+} sparks (~20 ms in cardiac myocytes) is strongly affected by both endogenous Ca^{2+} buffers and indicator properties in our model simulations. With the standard parameter set, the model spark decay time is ~25 ms (Fig. 1 *C*), while in simulations in which the Ca^{2+} indicator (50 μM) is the sole Ca^{2+}-binding species, $T_{1/2}^{decay}$ is reduced to 4 ms (Fig. 2 *C*). In contrast, if only a trace amount of fluo-3 (0.1 μM) is added to endogenous buffers, the result is 38 ms. These calculations indicate that *interaction* between endogenous buffers and the dye is a major contributor to the decay rate of elevated local fluorescence; that is, after the cessation of RyR flux, stationary buffers exposed to high Ca^{2+} discharge and act as a source of free Ca^{2+}, slowing the decay of Ca^{2+}-bound indicator. However, this effect is not a simple monotonic function of the buffer concentration. The maximum $T_{1/2}^{decay}$ shown in Fig. 2 *C* occurs in the presence of 5 rather than 10 times the standard concentration of endogenous buffer. Since buffer capacity alone can alter the decay rate more than an order of magnitude, it would be of interest for future study to correlate the decay rate with the abundance of physiological Ca^{2+} buffers in various cell types. Local Ca^{2+}

clearance by the SR Ca^{2+} ATPase had a small but noticeable contribution to the decline of fluorescence signal (Fig. 2 *D*), as was observed experimentally (Gómez et al., 1996). Furthermore, the decay rate was dependent on both release duration ($T_{1/2}^{decay}$ = 24–37 ms in Fig. 2 *A*) and Ca^{2+} release amplitude ($T_{1/2}^{decay}$ = 24–29 ms in Fig. 2 *B*).

Spark width: the full width at half maximum (FWHM)

As discussed above, using our standard parameter set the radial model predicts a FWHM that is about half the observed spark diameter. An unexpected feature of these calculations is that normalized spark breadth is not a strong function of the source amplitude (see Fig. 2 *B*). Indeed, most of the perturbations depicted in Fig. 2 have little effect on the FWHM of the simulated sparks. Total removal of the endogenous buffers produced the largest FWHM (1.3 μm at 10 ms), which is 50% larger than the standard value (Fig. 2 *C*) but still 30% smaller than a typical experimentally observed spark. Increasing stationary buffer capacity 10-fold decreased spark FWHM by only 8%. Varying Ca^{2+}-ATPase activity from 0× to 10× did not significantly decrease the FWHM. Spatially distributing Ca^{2+} release over a ring 0.6 μm in diameter, representing the entry of Ca^{2+} into the cytosol via the opening of a diad cleft, only slightly increased spark size (see Fig. 9 and related text). Even varying the dye parameters from the standard values listed in Tables 1 and 2, it is difficult to increase the FWHM of the model spark without simultaneously increasing its brightness beyond what is typically seen experimentally ($F/F_0 \sim 2.0$). Using the radial, isotropic simulation with a point source for Ca^{2+} release, we were able to achieve a typical experimentally observed FWHM (1.6 μm at 10 ms) while still maintaining $F/F_0 \approx 2$, but this required increasing both the PSF size and the source amplitude 3-fold (i_{Ca} = 6.0 pA, σ_z = 0.346 μm^2, and σ_{xy} = 0.087 μm^2, giving $FWHM_z$ of 2.4 μm and $FWHM_{xy}$ of 1.2 μm).

The role of the indicator dye in spark formation

As in our preliminary calculations (Smith et al., 1996), we find that the concentration and mobility of indicator can alter the decay rate of a Ca^{2+} spark event. Fig. 3 *A* shows that adding higher concentrations of indicator has the counterintuitive effect of reducing the peak F/F_0 as well as accelerating the decay rate. Fig. 3, *B* and *E* demonstrate that varying the mobility of fluo-3 dramatically changes both the spatial and temporal properties of the fluorescent signal. When 50 μM fluo-3 is totally immobilized (D_F = 0), the decay of fluorescence signal is extremely slow ($T_{1/2}^{decay}$ = 72 ms), and the peak fluorescence signal (at Y_{offset} = 0.5 μm and Z_{offset} = 0) increased by 18% (*panel B, top curve*) relative to the result obtained with D_F = 20 μm^2/s. Furthermore, the fluorescence signal (at $Y_{offset} = Z_{offset}$ = 0, t = 10 ms) saturated over a radius of ~300 nm and then sharply declined toward basal level (*panel E, top dashed line*). A higher diffusion coefficient reduces the peak F/F_0 (*panel B*) and allows the fluorescence signal to respond more quickly to the termination of Ca^{2+} release ($T_{1/2}^{decay}$ = 8 ms at D_F = 200 μm^2/s). These results show that indicator dye with even small mobility (here 20 μm^2/s) has behavior markedly distinct from that of a stationary version of the same dye. Thus, use of immobile dyes [e.g., conjugated to dextran beads or to membrane proteins (Horne and Meyer, 1997)] may have both advantages (e.g., brighter but not necessarily more confined in space) and disadvantages (e.g., distorted kinetics).

Fig. 3, *C* and *F* examine the effects of indicator kinetics at 0.1×, 0.5×, 1×, 2×, and 10× the nominal rate of fluo-3 while holding K_F constant. The simulated peak fluorescence change as a function of these rates (with lateral distance Y_{offset} = 0.5 μm) is 1.22, 1.72, 2.01, 2.24, and 2.43, respectively; and $T_{1/2}^{decay}$ is 49, 31, 25, 23, and 22 ms. These results indicate that, for a given dissociation constant (K_F), rapid indicators lead to both brighter sparks and faster spark decay rates. In addition, these calculations show that in all cases, $T_{1/2}^{decay}$ is not easily estimated from the Ca^{2+} dissociation time constant (i.e., 110, 22, 11, 5.5, and 1.1 ms); rather, Ca^{2+} fluxes from dye diffusion and discharge of the immobile endogenous buffer largely determine $T_{1/2}^{decay}$. Another simulation result that may be counterintuitive is that slow indicator dye rate constants can result in spatially restricted fluorescence signals (Fig. 3 *F*).

The indicator dye perturbs Ca^{2+} signaling

We have used the radial Ca^{2+} spark simulation to examine the extent to which the presence of an indicator dye perturbs the free Ca^{2+} signal. In Fig. 3 *D*, the Ca^{2+} profile in the absence of fluo-3 (outermost dashed line for Ca^{2+}) nearly overlaps the Ca^{2+} profile in the presence of 50 μM fluo-3, the estimated dye concentration in most spark experiments. This suggests that this concentration of indicator has a negligible effect on physiological Ca^{2+} signaling. However, as the amount of the dye increased to concentrations used in some recent studies (1–2 mM, Wang et al., 1997), free Ca^{2+} in regions distant (>100 nm) from the origin is suppressed in a dose-dependent manner, resulting in a spatially confined Ca^{2+} signal (Fig. 3 *D*). Conversely, the fluorescence signal broadens slightly with increasing dye concentrations (Fig. 3 *D*). These calculations suggest that Ca^{2+} coupling between the SL and the SR (which occurs on a distance scale of tens of nanometers) is unlikely to be affected by submillimolar concentrations of fluo-3, consistent with results using other Ca^{2+} chelators (Sham, 1997). Nevertheless, such concentrations of indicator may have a major effect on Ca^{2+} coupling between more distant sites, e.g., during sequential recruitment of release units and the propagation of Ca^{2+} waves (Parker et al., 1996; Cheng et al., 1996a; Lukyanenko et al., 1996).

An unexpected result of these calculations is that changing parameters other than the total dye concentration has little effect on the free Ca^{2+} profiles, as shown by the nearly

overlapping Ca^{2+} profiles in Fig. 3 *E* ($D_F = 0–200\ \mu m^2/s$) and Fig. 3 *F* ($k_F^+ = 8–800\ \mu M^{-1}s^{-1}$). Similar results were obtained for the time course of local [Ca^{2+}] transients (data not shown). These indicator dye properties, while largely determining the appearance of the fluorescence signal, do not dramatically influence the rate of free Ca^{2+} clearance (via facilitated diffusion) when the dye is present at low concentrations (50 μM throughout Fig. 3, *E* and *F*). Taken together, these calculations illustrate a dilemma confronting spark measurement and interpretation: fluorescence signals may not faithfully reflect changes in the underlying Ca^{2+} signal (Fig. 3 *D*) and vice versa (Fig. 3, *D* and *F*; see Fig. 7 and below for more examples).

What elevated fluorescence tells us about the Ca^{2+} signal

A Ca^{2+} spark is the experimentally measured elevation in fluorescence signal. We are interested in whether or not the true free Ca^{2+} signal can be derived from the fluorescence signal after correcting for distortions due to optical blurring. As shown in Fig. 4 *A*, the simulated fluo-3 fluorescence profile ([CaF] w/PSF at $Y_{offset} = Z_{offset} = 0$ and $t = 10$ ms, *heavy dotted line*) is a poor representation of the Ca^{2+} profile (*solid line*), even in the absence of any out-of-focus blurring (*light dotted line*). Furthermore, the Ca^{2+} profile back-calculated from the usual equilibrium formula applied to the blurred (*heavy dashed line*) or non-blurred (*light dashed line*) fluorescence profile still differs markedly from the simulated Ca^{2+} profile. Specifically, the back-calculated profile grossly underestimates [Ca^{2+}] near the origin, whereas in regions farther away (>0.5 μm in the example shown in Fig. 4), the fluorescence overestimates [Ca^{2+}]. Both errors are attributable to the lack of equilibrium of Ca^{2+} with the indicator and the presence of large gradients for Ca^{2+} and fluo-3 (in both Ca^{2+}-free and Ca^{2+}-occupied forms) (Smith et al., 1996).

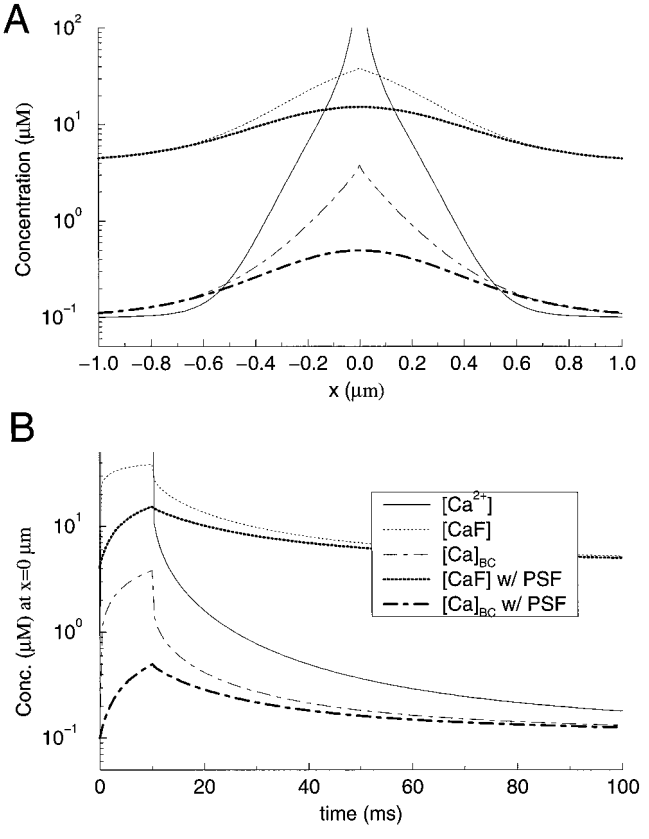

FIGURE 4 Back-calculation of [Ca^{2+}] from the fluorescence signal. (*A*) Simulated spatial profiles of [Ca^{2+}] (*solid line*), [CaF] (*thin dotted line*), [CaF] convolved with PSF (*thick dotted line*), and calculated [Ca^{2+}] using [CaF] with PSF (*thick dot-dashed line*) or [CaF] (*thin dot-dashed line*). $Y_{offset} = Z_{offset} = 0$ and $t = 10$ ms. (*B*) Time courses of these signals at $Y_{offset} = Z_{offset} = 0$.

Not only is the Ca^{2+} signal more confined in space, but it also decays much more rapidly than the fluorescence signal (Fig. 4 *B*, *solid line* versus *dotted lines*). Back-calculation assuming equilibrium between dye and Ca^{2+} (Fig. 4 *B*, *dashed lines*) underestimates the transient free Ca^{2+} elevation at origin of spark, both during release and after release has terminated. Fig. 4 demonstrates that by using the current generation of Ca^{2+} probes and confocal fluorescence technology, it is not possible to ascertain the true $[Ca^{2+}]_i$ signal from fluorescence measurements without quantitative modeling. Caution should be exercised in interpreting spatiotemporal dynamics of local Ca^{2+} on the basis of fluorescence measurement alone.

Spark statistics: intrinsic variance versus variance due to off-center sampling

Since both the confocal PSF and Ca^{2+} sparks have finite dimensions, sparks seen in line scan imaging include both in-focus and out-of-focus events, and to date no detection algorithm has been devised that can discriminate between them. However, simulations can help to reveal how random sampling may distort Ca^{2+} spark statistics. Although this question has been addressed previously (Pratusevich and Balke, 1996), our calculations can address whether the mobility of the indicator dye influences these conclusions. We are also interested in the relation between the apparent and the intrinsic spark statistics, a question which to our knowledge has not to date been examined.

Ca^{2+} release sites in cardiac cells are concentrated around *Z*-lines and exhibit a quasi-periodicity of ~1.8 μm in the longitudinal direction (Carl et al., 1995; Sun et al., 1995; Cheng et al., 1996a; Parker et al., 1996). However, no ultrastructural data show strict regularity in the transverse direction. The transverse regularity, if any, may not be in register over many sarcomeres, e.g., 30–50 sarcomeres typically surveyed in a single linescan image. Thus, it is reasonable to assume that Ca^{2+} sparks originate at sites distributed randomly and uniformly around the confocal scanline. Given this assumption, we systematically calculated spark parameters, including F/F_0, FWHM, and $T_{1/2}^{decay}$, as functions of the lateral (Y_{offset}) and axial (Z_{offset}) displace-

ment of the center of the PSF from the origin (*o*) of our standard Ca^{2+} spark (Fig. 5 *A*). The results are summarized as surface plots shown in Fig. 5, *B–D*. In general, off-center sparks have smaller amplitudes compared to the in-focus sparks (Fig. 5 *B*) while spark width (Fig. 5 *C*) and duration (Fig. 5 *D*) increases with larger Y_{offset} and Z_{offset}. If we further assume a detect threshold of peak $F/F_0 = 1.25$ due to the presence of noise (Pratusevich and Balke, 1996; Song et al., 1997), Fig. 5, *E–G* show the expected parametric distributions of a stereotyped event after random sampling

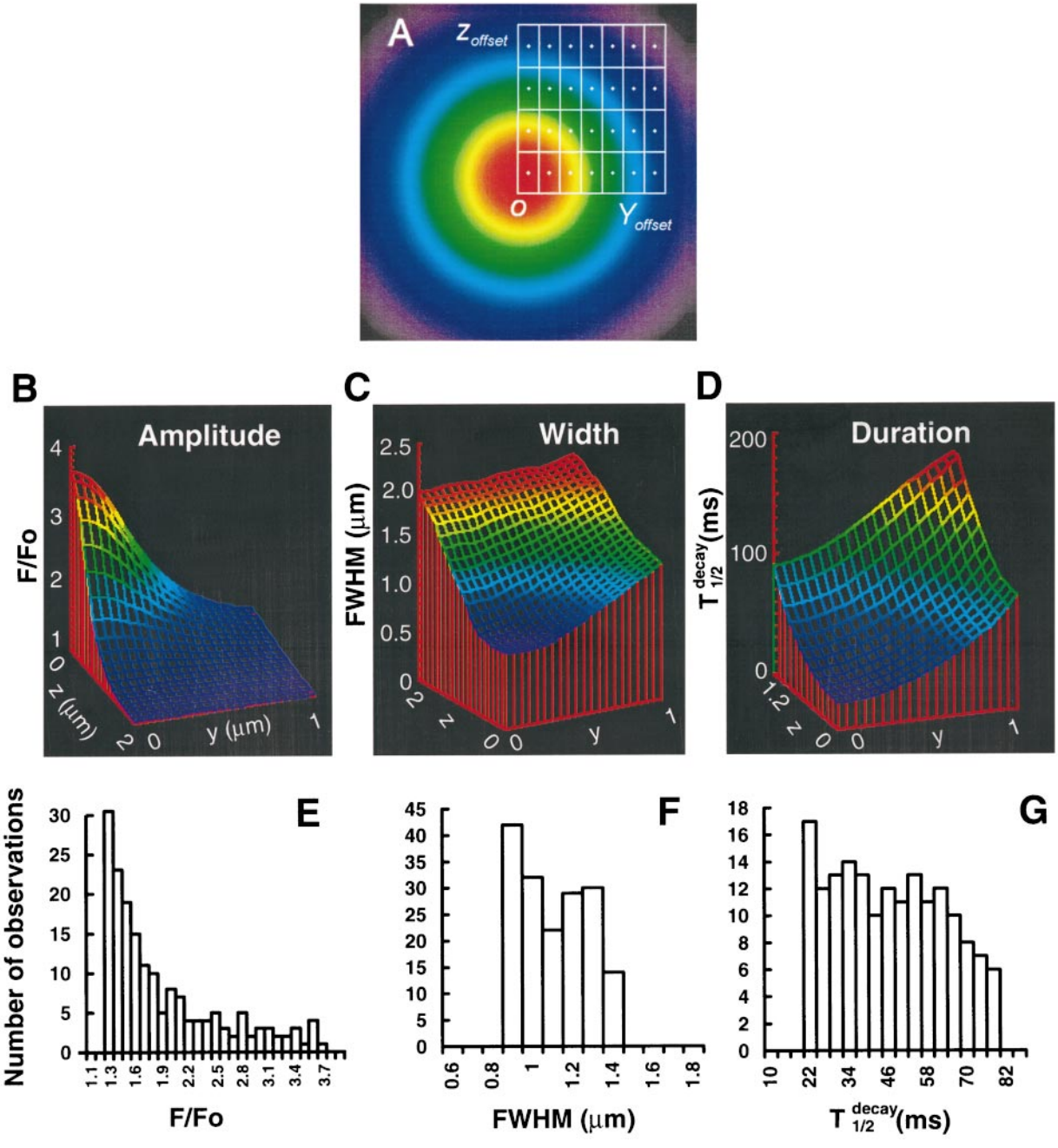

FIGURE 5 Effects of random off-center sampling on experimental parametric measurement of stereotypical Ca^{2+} sparks. (*A*) Position of scan lines in relation to Ca^{2+} sparks. Side view of scan lines (*crosses*) running across Ca^{2+} sparks (*shaded areas*) originated at point O. Direction of linescan is perpendicular to the section plane. A scan line can run right through the spark origin, or more likely, be displaced either laterally (Y_{offset}), or vertically (Z_{offset}), or in both directions. If the scanning line is positioned randomly with respect to the origin of the Ca^{2+} spark and the spark is spherically symmetric, we expect the distribution of linescan locations to be uniformly distributed across the section plane. (*B–D*) Surface plots of spark amplitude (*B*), width at peak F/F_0 (*C*) and half-decay time, $T^{decay}_{1/2}$ (*D*) as a function of scan line position (*y*, *z*). (*E–G*) Histogram distributions of spark parameters after random sampling. As shown in *panel A*, the scan line was placed at regular, discrete locations, with Y_{offset} and Z_{offset} varying from 0–1 μm and 0–2 μm at increments of 0.05 μm and 0.1 μm, respectively. A spark was calculated at each location and the statistics shown are for sparks after thresholding at $F/F_0 = 1.25$. Plots are for F/F_0 (*E*), FWHM (*F*), and $T^{decay}_{1/2}$ (*G*).

via confocal linescan imaging. All spark parameters exhibit broad distributions with F/F_0 of 1.9 ± 0.6 (mean ± SD), FWHM of 1.1 ± 0.2 μm, and $T_{1/2}^{decay}$ of 48.2 ± 16.7 ms. The time to peak fluorescence also increased with distance (data not shown) and had a mean value of 14.6 ± 3.1 ms, which overestimates the Ca^{2+} release duration by 46% (10 ms). These calculations are in general agreement with those of Pratusevich and Balke (1996).

Given the transfer functions for spark measurement via confocal imaging (e.g., Fig. 5, *E–G*), what apparent spark statistics should be expected? In our model, the transfer function for spark amplitude follows a monotonic distribution. If multiple populations of Ca^{2+} sparks coexist, our model still predicts a monotonic decreasing function for observed spark amplitudes, as long as the apparent amplitude distribution of each subpopulation is a monotonic decreasing function.

In principle, it is possible to back-calculate the intrinsic spark statistics via a deconvolution algorithm using model-derived transfer functions. In practice, the large variance due to detection (Fig. 5; Pratusevich and Balke, 1996) as well as to photon noise (Pratusevich and Balke, 1996) severely comprises our ability to do so. In the simplest case, if all variance in spark statistics were explainable by off-center sampling of a stereotypical event, our model predicts strong intercorrelation among three spark parameters: a strong positive correlation between duration and width (γ_1, 0.99) and a strong negative correlation between peak and duration (γ_2, −0.88), or width (γ_3, −0.88). To the contrary, experimental data reveal only weak correlation that is sometimes in the opposite direction (γ_1 = 0.16, γ_2 = −0.18, γ_3 = 0.37) (Song et al., 1997). This important negative result indicates that not all sparks are stereotypical and that there must be intrinsic variation among individual release events. Intrinsic variance might be expected on the grounds of stochastic gating of RyR, even if a spark is a collective phenomenon of a cluster of RyR's (Stern, 1992a,b).

Effects of intrasarcomeric inhomogeneities, anisotropic diffusion, and the geometry of the Ca^{2+} release site

To investigate the role of spatial inhomogeneities in the shaping of Ca^{2+} sparks, we carried out further experiments and simulations using the cylindrical version of our model of Ca^{2+} spark formation and detection. Fig. 6 *A* shows a representative confocal image of a rat ventricular myocyte stained with immunofluorescence against the cardiac Ca^{2+}-ATPase, SERCA2. In its enlarged view (Fig. 6 *B*), the signal is concentrated along the *Z*-lines of sarcomeres. Fig. 6 *C* plots the average sarcomeric distribution pattern (*curve a*), which is fit well by a Gaussian function (*curve b*). After deconvolution using our standard PSF parameters to remove

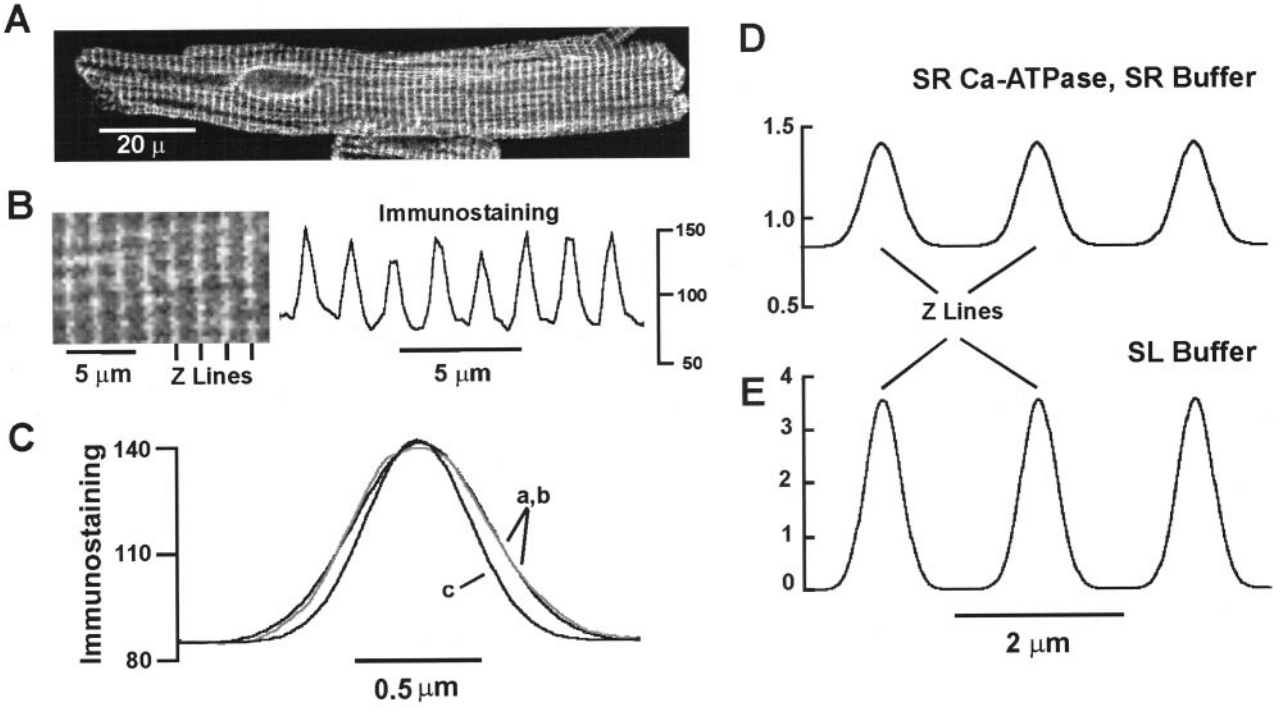

FIGURE 6 Inhomogeneities of Ca^{2+} handling mechanisms. (*A*) A representative immunostaining of rat ventricular myocytes with anti-SERCA2 primary antibody. (*B*) Enlarged view of eight sarcomeres in *panel A* (*left*) and the corresponding plot of immunofluorescence distribution (*right*). Positions of *Z*-lines are as indicated. Sarcomere length is 1.8 μm. (*C*) Average immunofluorescence distribution over a sarcomere (*gray line, a*), its Gaussian fit (*dark line, b*), and the fitted profile after deblurring using the PSF in Eq. 9 (*c*). (*D–E*) Hypothetical function for subsarcomeric distribution of SR Ca^{2+} pump and SR buffer (*D*) and SL buffer (*E*). These curves are scaled from *curve c* in *panel C*, with (*D*) and without (*E*) the basal constant component. In all cases, the value averaged over an entire sarcomere is unity.

optical blurring, the result (*curve c*) consists of two components: a uniform background component reflecting the contribution of the longitudinal SR, and a local bell-shaped component centered around the *Z*-line that probably reflects the average distribution of the pump at terminal SR. For purposes of the simulation, curve *c* is used to represent the intrasarcomeric distribution of the Ca^{2+} pump as well as SR membrane Ca^{2+} buffer (Fig. 6 *D*). We further hypothesize that average sarcolemmal (*t*-tubule) membrane buffer follows the pattern of the local component of the SR but with the background component set to zero (Fig. 6 *E*).

Representative results of the cylindrical simulations incorporating these longitudinal inhomogeneities are shown in Fig. 7. Because Ca^{2+} release occurs at the *Z*-line (Shacklock et al., 1995; Cheng et al., 1996a), one consequence of the nonuniform distribution of membrane Ca^{2+} buffers and SR Ca^{2+} pumps is to restrict the Ca^{2+} profile 10–20% in the transverse (*Z*-plane) as compared to the longitudinal direction. In contrast, there was virtually no directional difference for the fluorescence profile, underscoring the fact that fluorescence signals do not always respond to changes in the free Ca^{2+} profile. Retrospectively, this result is expected since any directional difference in free Ca^{2+} will be attenuated by the diffusion of [CaF]. The observation that sparks are ~20% larger in the long axis than in the short axis of the cell (Cheng et al., 1996b; Parker et al., 1996) must be due to other reasons (e.g., anisotropy in diffusion of Ca^{2+} and/or the dye). Fig. 7 also compares these inhomogeneous simulations with the corresponding homogeneous calculation (i.e., a simulation using identical but spatially averaged values for all parameters). In both the transverse and longitudinal directions, the inhomogeneous simulation predicts a more restricted spreading of the Ca^{2+} and fluorescence signals and a moderate reduction in signal amplitude. Presumably this is due to the presence of Ca^{2+} removal mechanisms (e.g., membrane buffers, pumps) that are preferentially localized near the *Z*-line in the inhomogeneous simulation. Apart from this small directional difference in Ca^{2+}, no further qualitative difference was observed between the homogenous and inhomogeneous versions of the model.

Results on anisotropic diffusion are shown in Fig. 8. Reduction of the transverse diffusion coefficient of either Ca^{2+} (D_C, *panel B*) or dye (D_F, *panel C*) or both (*panel D*) by 50% leads to a shrinkage in the transverse direction and an expansion of spark in the longitudinal direction, as compared to the isotropic example shown in panel *A*. (The longitudinal expansion occurs without an increase in the longitudinal diffusion coefficient and reflects diffusion of Ca^{2+} preferentially channeled in the direction of least resistance.) Both shrinkage and expansion effectively reproduce the oblong shape of Ca^{2+} spark appearance: the eccentricity of sparks (see legend) in panels *B*, *C*, and *D* are 1.18, 1.18, and 1.36, respectively. A directional difference in the Ca^{2+} profile was also observed under these conditions (data not shown). Taken together, these calculations and those of the previous paragraph suggest that the asymmetric shape of Ca^{2+} sparks is more likely due to anisotropic diffusion of both indicator dye and free Ca^{2+} ions (or possibly indicator dye alone), rather than subsarcomeric inhomogeneities of the Ca^{2+} buffer and transport system. The microscopic asymmetry of elementary Ca^{2+} signaling, albeit small, may be the cause of experimentally observed anisotropies in macroscopic $[Ca^{2+}]_i$ dynamics. For example, Ca^{2+} waves in heart cells propagate 30% to 55% faster longitudinally than transversely (Engel et al., 1994) even though release sites are separated, on average, about three times farther apart in this direction (Carl et al., 1995; Parker et al., 1996).

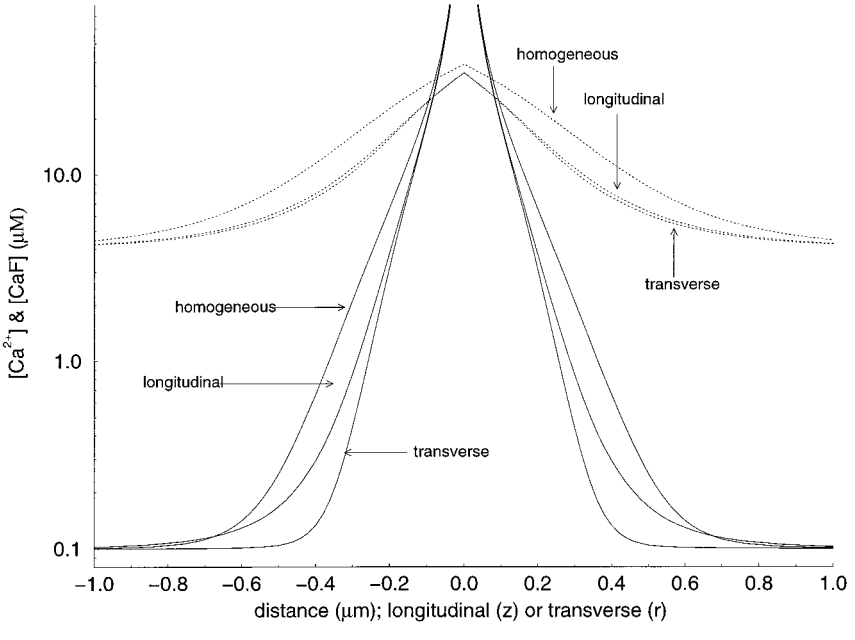

FIGURE 7 Simulations comparing $[Ca^{2+}]$ (*solid lines*) and [CaF] (*dotted lines*) profiles at $t = 10$ ms for homogeneous and inhomogeneous versions of the model. Traces labeled *homogeneous* are identical to the $[F]_T = 50\ \mu M$ traces shown in Fig. 3 *D*. Traces labeled *longitudinal* and *transverse* are the results of the inhomogeneous (cylindrical) simulation. See text for the model. Note that the $[Ca^{2+}]$ profile of the inhomogeneous model is restricted in both longitudinal and transverse directions, but more so in the *transverse* direction, in which total endogenous buffer concentration is highest. On the other hand, this directional difference is not clearly seen in the [CaF] traces, as the mobility of the indicator dye results in a smoothing of the CaF signal.

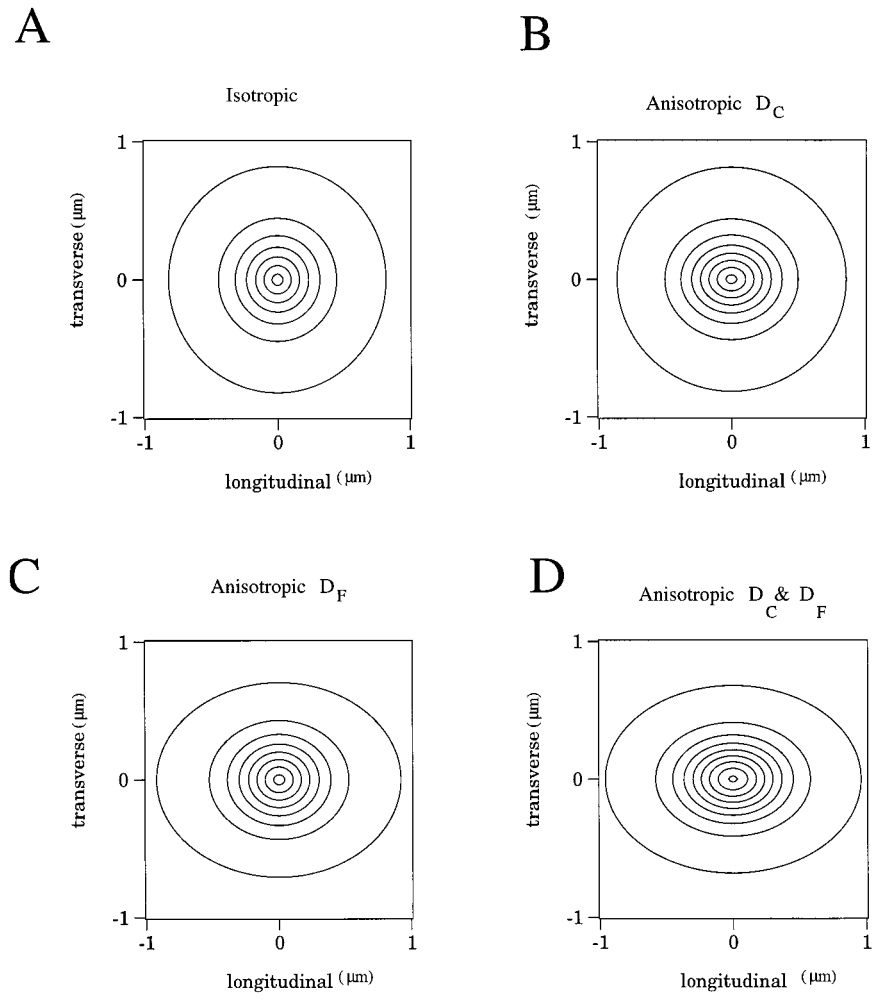

FIGURE 8 Role of anisotropic diffusion on the appearance of Ca^{2+} sparks. Simulated Ca^{2+} sparks using standard (*A*) or 50% reduced values for the diffusion coefficient of Ca^{2+} (*B*) or indicator dye (*C*) or both (*D*) in the transverse direction, while keeping the standard values of D_C and D_F in the longitudinal direction. Isoconcentration curves (*solid lines*) are shown for [CaF] = 5 (outermost), 10, 15, 20, 25, 30, 35, 40, and 45 μM. Calculation does not include spatial averaging due to PSF. A measure of the longitudinal extent of the spark (L_Z), defined as the longitudinal extent of the [CaF] = 10 μM isoconcentration curve (second outermost), as well as the transverse extent (L_R, here the smaller value), and eccentricity ($E = L_Z/L_R$) are presented for each calculation. (*A*) *Isotropic:* neither D_C nor D_F reduced; peak [CaF] = 38.7 μM and both L_Z and L_R are 0.96 μm, giving eccentricity (E) of 1.0. (*B*) *Anisotropic* D_C. D_C, but not D_F, is reduced in transverse direction. Peak [CaF] = 43.1 μM, L_Z = 1.08 μm, L_R = 0.92 μm, E = 1.17. (*C*) *Anisotropic* D_F: D_F but not D_C is reduced in transverse direction. Peak [CaF] = 43.3 μM, L_Z = 1.02 μm, L_R = 0.92 μm, E = 1.21. (*D*) *Anisotropic* D_C and D_F: both D_C and D_F are reduced in transverse direction. Peak [CaF] = 46.7 μM, L_Z = 1.24 μm, L_R = 0.88 μm, E = 1.41. Note that the *anisotropic* D_F case is slightly more eccentric than the *anisotropic* D_C case, and that a 50% reduction in either diffusion coefficient alone results in the experimentally observed eccentricity of 20% (Cheng et al., 1996).

We also used the cylindrical version of our model of Ca^{2+} spark formation and detection to investigate the role of the geometry of the Ca^{2+} release site on the shape of Ca^{2+} sparks. For example, Fig. 9 *A* shows isoconcentration curves (*solid lines*) for the CaF profile of a simulated Ca^{2+} spark using standard parameters, except that Ca^{2+} release is spatially distributed over a ring 0.6 μm in diameter, representing the entry of Ca^{2+} into the cytosol via the opening of a diad cleft. When spatial averaging due to the PSF is not included (Fig. 9 *A*), the CaF profile responds to the geometry of the Ca^{2+} release and the spatially extended source creates a spark that is elongated in the plane of the ring. However, when spatial averaging is included (e.g., using a spherical PSF with FWHM = 0.4 μm in Fig. 9 *B* and 0.6 μm in Fig. 9 *C*), the ring geometry of the source is obscured and the eccentricity of the Ca^{2+} spark is reduced. In addition, the ring geometry of the source in these cylindrical simulations produces only a modest increase in the FWHM of the spark in the plane of the ring ($FWHM_R$ = 1.04 μm in Fig. 9 *B* and 1.08 μm in Fig. 9 *C*). Considering the source diameter was increased by 0.6 μm, these values represent only a small increase in the FWHM over that of the standard spherical spark of Fig. 1 *D* (FWHM = 0.89 μm). Once again, we observe that the FWHM is a Ca^{2+} spark measure that is relatively insensitive to model parameters.

DISCUSSION

Although the problem of Ca^{2+} diffusion from open channel mouth into buffer-containing medium has been studied by many investigators (e.g., Stern, 1992a,b; Langer and Peskoff, 1996; Soeller and Cannell, 1997), the present work shows that in the context of fluorescent measurement, the Ca^{2+} signal may not be directly translated into the signal reported by the indicator, and that the Ca^{2+} signal per se may be altered by the presence of the indicator. The present model of Ca^{2+} spark formation explicitly solves equations for the diffusion of both free Ca^{2+} and indicator (Cheng et al., 1993, 1995; Gómez et al., 1996). There are two major differences in the model reported here when compared to the model of Pratusevich and Balke (1996): 1) the present work emphasizes Ca^{2+} spark *formation* mechanisms and also the relation between the increase in fluorescence and the elevation of the underlying $[Ca^{2+}]_i$, issues complementary to those involved in spark *detection*, such as optical

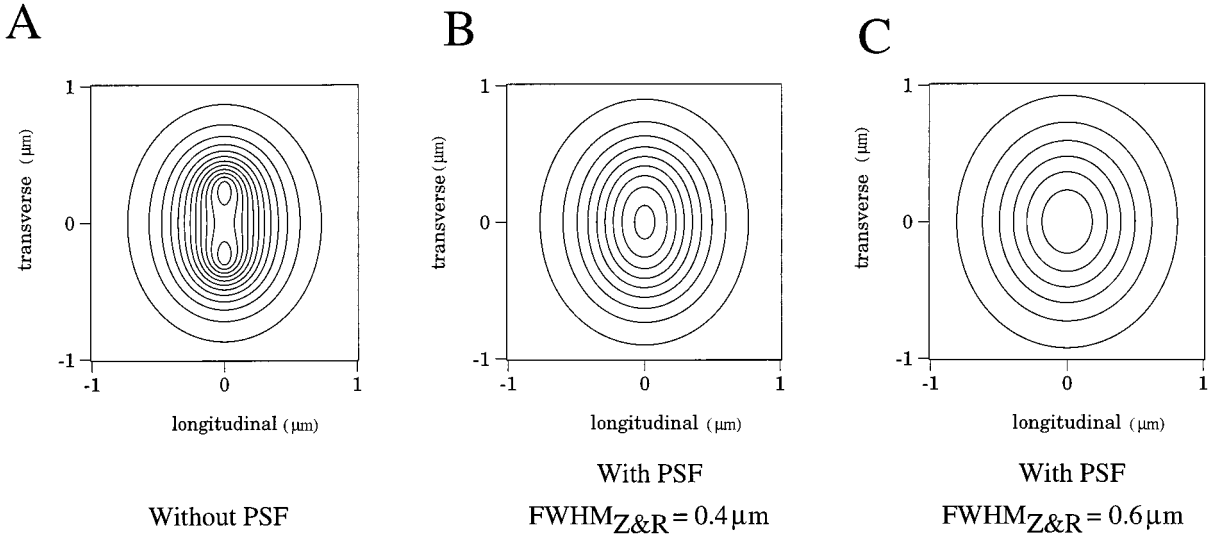

FIGURE 9 Simulated Ca^{2+} spark using standard parameters except that Ca^{2+} release is spatially distributed over a ring 0.6 μm in diameter, representing the entry of Ca^{2+} into the cytosol via the opening of a diad cleft. Isoconcentration curves (*solid lines*) are shown for [CaF] of 5 μM and successively higher concentrations at 1 μM intervals. A measure of the longitudinal extent of the spark (L_Z), defined as the longitudinal extent of the [CaF] = 10 μM isoconcentration curve, as well as the transverse extent (L_R, here the larger value), and eccentricity ($E = L_Z/L_R$) are presented for each calculation. Time is 10 ms. (*A*) This calculation does not include spatial averaging due to PSF. Note that one consequence of distributing the Ca^{2+} release over a ring 0.6 μm in diameter is to create a spark which is elongated in the plane of the ring (L_Z = 0.60 μm, L_R = 0.96 μm, and $E = L_Z/L_R$ = 0.63). The innermost isoconcentration curves indicate [CaF] = 16 μM. (*B*) Calculation shown in (*A*) after spatial averaging with a spherical PSF ($FWHM_{xy}$ = 0.4 μm and $FWHM_z$ = 0.4 μm) giving L_Z = 0.56 μm, L_R = 0.80 μm, and E = 0.70. Innermost isoconcentration curve indicates [CaF] = 13 μM and the FWHM of the simulated Ca^{2+} spark in the longitudinal and transverse directions is 1.04 and 0.76 μm, respectively. (*C*) Calculation shown in (*A*) after spatial averaging with a larger spherical PSF ($FWHM_{xy}$ = 0.6 μm and $FWHM_z$ = 0.6 μm) giving L_Z = 0.36 μm, L_R = 0.44 μm, and E = 0.82. Innermost isoconcentration curve indicates [CaF] = 10 μM and the FWHMs of the simulated Ca^{2+} spark in the longitudinal and transverse directions are 1.08 and 0.92 μm, respectively, slightly greater than (*B*). Note that in both (*B*) and (*C*), out-of-focus fluorescence interferes with resolving the geometry of the source and that low resolution (larger PSF) reduces the observed eccentricity, i.e., E is closest to unity in (*C*). Also note that the ring geometry of the source in this cylindrical simulation increases the FWHM of the spark only slightly over the standard spherical spark of Fig. 1 *D*, where FWHM = 0.89 μm.

blurring, photon noise, and detectability; 2) the mobility of the indicator dye is included as factor in the model presented here. As shown in Fig. 3, neglect of dye diffusion altogether introduces large errors in the amplitude, time to peak, relaxation, and spatial spreading of the simulated spark. In the previous model, an extremely high SR Ca^{2+}-ATPase activity (spatially averaged V_{max} ~44,444 μM/s vs. 208 μM/s reported in Bassani et al., 1994) and a high free Ca^{2+} diffusion coefficient (600 μm^2/s) compensates for the effect of dye immobilization. Furthermore, their model assumes a latticelike distribution of RyR's, a discrete distribution of the SR pump on longitudinal and transverse planes separated 0.675 μm apart, and a discontinuity of Ca^{2+} diffusion coefficient across these planes. The scenarios of spark formation mechanisms presented in the two models are thus very different. Computationally, their choice of geometry requires a 3-D simulation (with eightfold symmetry), whereas the simplicity of the present model allows us to comprehensively explore different parameter settings. In both the present model and the model by Pratusevich and Balke, details on structure, Ca^{2+} binding, and surface charges inside the diad cleft, where junctional RyR's reside, have not been included. The importance of these nanoscale features in the establishment and dissipation of Ca^{2+} gradient *within* the diadic space has recently been modeled in the context of cardiac excitation-contraction coupling (Soeller and Cannell, 1997) and Ca^{2+} extrusion via the SL Na^+/Ca^{2+} exchange (Langer and Peskoff, 1996).

The model of Pratusevich and Balke (1996) predicts a monotonic spark amplitude distribution when the observation line is positioned randomly with respect to the origin of the spark (see also Fig. 5 *E*), but a multimodal distribution when repeated observations of randomly occurring sparks are made from the same scan line. The latter seems to stem from their assumption that release sites form a rigorous lattice in *Z*-planes and that the pattern is strictly in register over all *Z*-planes (which is unlikely inside the cell). While observations in which sparks were selected by eye have often indicated an amplitude distribution consisting of one or more Gaussian components (Klein et al., 1996; Lukyanenko et al., 1996; Satoh et al., 1997; Xiao et al., 1997), more recent studies suggest another explanation for the experimentally observed modal distribution. With automated computer algorithms to count and measure Ca^{2+} sparks, about twice as many Ca^{2+} sparks (often in the low amplitude end) can now be detected and the amplitude distributions in both cardiomyocytes (Song et al., 1997) and skeletal muscle cells (E. Rios, personal communication) are consistent with a monotonic decreasing function, subjected to detection thresholding. This is consistent with the results

presented here and suggests that reported modal distributions could be due to the observer's selection bias against small amplitude events (rather than to ultrastructural regularity). Additionally, spark statistics may have multiple modes when the assumption of randomness is violated, e.g., statistics dominated by events from some particular sites exhibiting repetitive activities (Cheng et al., 1993; Tsugorka et al., 1995; Parker et al., 1996).

In the present study, we have demonstrated that a simple numerical model provides a very useful investigative tool for understanding the mechanism of Ca^{2+} spark formation and detection. Many salient features of Ca^{2+} sparks, including the amplitude, the kinetics, the oblong shape, as well as the modulation by physiological factors, are reproduced using the radial and cylindrical versions of the model. However, we have been unable to quantitatively reproduce the spatial size of the Ca^{2+} spark, indicating that our understanding of spark formation, as reflected in the model's structure and parameters, is still limited. More importantly, our calculations reveal three generic problems confronting the interpretation of fluorescence signal: 1) the fluorescence signal differs markedly from the underlying Ca^{2+} signal; 2) interpretation of fluorescence data (e.g., peak intensity) can be equivocal; and 3) differences seen in the fluorescence signal do not always match changes in Ca^{2+} signal, and it is equally true that not all changes in Ca^{2+} signal are accompanied by a similar change in fluorescence signal. Furthermore, the model cautions us that near millimolar concentrations of fluo-3-like indicator could disturb the Ca^{2+} signaling process of interest. Since indicator fluorescence has a complicated relationship to the underlying Ca^{2+} fluxes, and since Ca^{2+} spark statistics are contaminated with large variance due to limitations of contemporary confocal microscopy, computer modeling plays an important role in data interpretation and experiment design. Meanwhile, a new generation of Ca^{2+} indicators and optical techniques is required to resolve microscopic and nanoscopic Ca^{2+} signaling on the millisecond scale.

APPENDIX: NUMERICAL METHODS

The Laplacian operator simplifies in the case of cylindrical symmetry to

$$\nabla^2 = \frac{1}{r}\frac{\partial}{\partial r}\left(r\frac{\partial}{\partial r}\right)\hat{r} + \frac{\partial^2}{\partial z^2}$$
$$\hat{z} = \left(\frac{\partial^2}{\partial r^2} + \frac{1}{r}\frac{\partial}{\partial r}\right)\hat{r} + \frac{\partial^2}{\partial z^2}\hat{z} \qquad (r > 0) \tag{a1}$$

We can deal with the singularity of the polar form of the Laplacian at $r = 0$ by replacing Eq. a1 with it's Cartesian equivalent, $\nabla^2 = (\partial^2/\partial x^2)\hat{x} + (\partial^2/\partial y^2)\hat{y} + (\partial^2/\partial z^2)\hat{z}$. Cylindrical symmetry implies that the first two components of the Cartesian Laplacian have equal magnitudes. This allows us to approximate the polar Laplacian at the origin by

$$\nabla^2 \approx 2\frac{\partial^2}{\partial r^2}\hat{r} + \frac{\partial^2}{\partial z^2}\hat{z} \qquad (r = 0)$$

(see pp. 75–76 of Smith, 1985). Thus we can write

$$L(U^n_{0,j}) = \frac{2}{\Delta r^2}[2U^n_{1,j} - 2U^n_{0,j}] + \frac{1}{\Delta z^2}[U^n_{0,j+1} - 2U^n_{0,j} + U^n_{0,j-1}] \tag{a2}$$

for $i = 0$,

$$L(U^n_{i,0}) = \frac{1}{r_i \Delta r^2}[r_{i+1/2}(U^n_{i+1,j} - U^n_{i,j}) - r_{i-1/2}(U^n_{i,j} - U^n_{i-1,j})] + \frac{1}{\Delta z^2}[2U^n_{i,1} - 2U^n_{i,0}] \tag{a3}$$

for $j = 0$, and

$$L(U^n_{i,j}) = \frac{1}{r_i \Delta r^2}[r_{i+1/2}(U^n_{i+1,j} - U^n_{i,j}) - r_{i-1/2}(U^n_{i,j} - U^n_{i-1,j})] + \frac{1}{\Delta z^2}[U^n_{i,j+1} - 2U^n_{i,j} + U^n_{i,j-1}] \tag{a4}$$

for $i > 0$ and $j > 0$, where $U^n_{i,j}$ is an approximation to the function $u(r_i, z_j, t_n)$, u represents any of the species in Eqs. 2–4, $r_i = i\Delta r$, $z_j = j\Delta z$, $t_n = n\Delta t$, $L(U^n_{i,j})$ is the approximation to the Laplacian at the point (r_i, z_j, t_n), and we have used a "reflective" boundary condition $(\partial u/\partial r)|_{r=0} = 0$, in its discretized form, $U^n_{-1} = U^n_1$. For all species save Ca^{2+}, this boundary condition can be interpreted as a "no flux" condition at the origin, meaning that no mobile species can be transported via diffusion either into or out of the domain of the simulation. In the case of Ca^{2+}, the free species is introduced at the origin in accordance with the time-dependence of σ_{ryr} so that $\lim_{r\to 0}\{-2\pi r^2 D_c(\partial[Ca^{2+}]/\partial r)\} = \sigma_{ryr}$ is always satisfied, that is, at each time step we increase the concentration of Ca^{2+} at the origin ($[Ca^{2+}]_0$), at a rate in accordance with the reaction term $J_{ryr} = \sigma_{ryr}\delta(\vec{r})$. The rate of change in Ca^{2+} concentration at the origin due to the presence of the source (σ_{ryr}) depends on the source strength and the volume which the mesh point at the origin "represents," that is, a cylinder with radius $\Delta r/2$ and height $\Delta z/2$, with volume $V = \pi(\Delta r/2)^2(\Delta z/2)$. Using Faraday's law, $\sigma_{ryr} = i_{Ca}/2F$, where i_{Ca} is the current amplitude of the source, and F is Faraday's constant ($F = 9.648 \times 10^4$ coul/mol), the rate of change in $[Ca^{2+}]$ at the origin due to the presence of the release site is

$$J_{ryr} = \frac{\sigma_{ryr}}{V} = \frac{8i^*_{Ca}(5.128 \times 10^3\ \mu M\ s^{-1})}{\pi(\Delta r^*)^2 \Delta z^*} \tag{a5}$$

where i^*_{Ca} is the source strength measured in picoamps, and Δr^* and Δz^* are the mesh size measured in micrometers.

Using the above equations, an explicit numerical scheme that is second-order accurate in space and first-order accurate in time is given by

$$\frac{U^{n+1}_{i,j} - U^n_{i,j}}{\Delta t} = D_u L(U^n_{i,j}) + RXN(U^n_{i,j}) \tag{a6}$$

where D_u is the diffusion constant for species u and $RXN(U^n_{i,j})$ denotes the contribution of the appropriate reaction terms in Eqs. 2–4. Of course, $L(U^n_{i,j})$ evaluates to zero when u denotes a stationary Ca^{2+} buffer, since in that case $D_u = 0$.

These calculations were performed on a Silicon Graphics Indigo 2 workstation. In addition to the explicit numerical scheme presented here, we coded a second version using an alternate direction implicit numerical scheme that produced identical results.

The authors thank Mark B. Cannell for initial discussion on spark modeling, C. F. Neubauer for experiments with immunofluorescence, and Arthur Sherman and Edward G. Lakatta for reading this manuscript.

This work is supported by National Institutes of Health intramural research programs (to H.C. and M.D.S.), a National Institutes of Health IRTA fellowship (to G.S.), National Institutes of Health grants (to J.K. and W.J.L.), and the Agricultural Experiment Station at University of California Davis (J.K.).

REFERENCES

Allbritton, N. L., T. Meyer, and L. Stryer. 1992. Range of messenger action of Ca^{2+} ion and inositol 1,4,5-trisphosphate. *Science.* 258:1812–1815.

Balke, C. W., T. M. Egan, and W. G. Wier. 1994. Processes that remove calcium from the cytoplasm during excitation-contraction coupling in intact rat heart cells. *J. Physiol. (Lond.).* 474:447–472.

Bassani, J. W. M., R. A. Bassani, and D. M. Bers. 1994. Relaxation in rabbit and rat cardiac cells: species-dependent differences in cellular mechanisms. *J. Physiol. (Lond.).* 476:279–293.

Berridge, M. 1993. Inositol trisphosphate and calcium signaling. *Nature.* 361:315–325.

Bers, D. M. 1991. Excitation-Contraction Coupling and Cardiac Contractile Force. Kluwer Academic Publishers, The Netherlands.

Bers, D. M., K. D. Philipson, and A. Peskoff. 1985. Calcium at the surface of cardiac plasma membrane vesicles: cation binding, surface charge screening, and Na-Ca exchange. *J. Membr. Biol.* 85:251–261.

Blatter, L. A., J. Hüser, and E. Riós. 1997. Sarcoplasmic reticulum Ca^{2+} release flux underlying Ca^{2+} sparks in cardiac muscle. *Proc. Natl. Acad. Sci. USA.* 94:4176–4181.

Cannell, M. B., H. Cheng, and W. J. Lederer. 1995. The control of calcium release in heart muscle. *Science.* 268:1045–1049.

Carl, S. L., K. Felix, A. H. Caswell, N. R. Brandt, W. J. Ball, Jr., P. L. Vaghy, G. Meissner, and D. G. Ferguson. 1995. Immunolocalization of sarcolemmal dihydropyridine receptor and sarcoplasmic reticular triadin and ryanodine receptor in rabbit ventricle and atrium. *J. Cell Biol.* 129:673–682.

Cheng, H., M. B. Cannell, and W. J. Lederer. 1995. Partial inhibition of Ca^{2+} current by methoxyverapamil (D600) reveals spatial nonuniformities in $[Ca^{2+}]_i$ during excitation-contraction coupling in cardiac myocytes. *Circ. Res.* 76:236–241.

Cheng, H., W. J. Lederer, and M. B. Cannell. 1993. Calcium sparks: elementary events underlying excitation-contraction coupling in heart muscle. *Science.* 262:740–744.

Cheng, H., M. R. Lederer, W. J. Lederer, and M. B. Cannell. 1996a. Calcium sparks and $[Ca^{2+}]_i$ waves in cardiac myocytes. *Am. J. Physiol.* 270:C148–C159.

Cheng, H., M. R. Lederer, R.-P. Xiao, A. M. Gómez, Y.-Y. Zhou, B. Ziman, H. Spurgeon, E. G. Lakatta, and W. J. Lederer. 1996b. Excitation-contraction coupling in heart: new insights from Ca^{2+} sparks. *Cell Calcium.* 20:129–140.

Eberhard, M., and P. Erne. 1989. Kinetics of calcium binding to fluo-3 determined by stopped-flow fluorescence. *Biochem. Biophys. Res. Commun.* 163:309–314.

Engel, J., M. Fechner, A. J. Sowerby, S. A. E. Finch, and A. Stier. 1994. Anisotropic propagation of Ca^{2+} waves in isolated cardiomyocytes. *Biophys. J.* 66:1756–1762.

Fabiato, A. 1985. Time- and calcium-dependence of activation and inactivation of calcium-induced release of calcium from the sarcoplasmic reticulum of a skinned cardiac Purkinje cell. *J. Gen. Physiol.* 85: 247–290.

Gómez, A., H. Cheng, W. J. Lederer, and D. M. Bers. 1996. Ca^{2+} diffusion and sarcoplasmic reticulum transport both contribute to $[Ca^{2+}]_i$ decline during Ca^{2+} sparks in rat ventricular myocytes. *J. Physiol. (Lond.).* 496:575–581.

Harkins, A. B., N. Kurebayashi, and S. M. Baylor. 1993. Resting myoplasmic free calcium in frog skeletal muscle fibers estimated with fluo-3. *Biophys. J.* 65:865–881.

Horne, J. H., and T. Meyer. 1997. Elementary calcium-release units induced by inositol trisphosphate. *Science.* 276:1690–1693.

Kieval, R. S., R. J. Bloch, G. E. Lindenmayer, A. Ambesi, and W. J. Lederer. 1992. Immunofluorescence localization of the Na-Ca exchanger in heart cells. *Am. J. Physiol.* 263:C545–C550.

Klein, M. G., H. Cheng, L. F. Santana, Y.-H. Jiang, W. J. Lederer, and M. F. Schneider. 1996. Two mechanisms of quantized calcium release in skeletal muscle. *Nature.* 379:455–458.

Langer, G. A., and A. Peskoff. 1996. Calcium concentration and movement in the diadic cleft space of the cardiac ventricular cell. *Biophys. J.* 70:1169–1182.

Lipp, P., and E. Niggli. 1996. Submicroscopic calcium signals as fundamental events of excitation-contraction coupling in guinea-pig cardiac myocytes. *J. Physiol. (Lond.).* 492:31–38.

López-López, J. R., P. S. Shacklock, C. W. Balke, and W. G. Wier. 1995. Local calcium transients triggered by single L-type calcium channel currents in cardiac cells. *Science.* 268:1042–1045.

Lukyanenko, V., I. Györke, and S. Györke. 1996. Regulation of calcium release by calcium inside the sarcoplasmic reticulum in ventricular myocytes. *Pflügers Arch.* 432:1047–1054.

Morton, K. W., and D. F. Mayers. 1994. Numerical Solution of Partial Differential Equations: An Introduction. Cambridge University Press, Cambridge, UK.

Neher, E. 1986. Concentration profiles of intracellular Ca^{2+} in the presence of diffusible chelator. *Exp. Brain Res.* 14:80–96.

Nelson, M. T., H. Cheng, M. Rubart, L. F. Santana, A. D. Bonev, H. J. Knot, and W. J. Lederer. 1995. Relaxation of arterial smooth muscle by calcium sparks. *Science.* 270:633–637.

Parker, I., and Y. Yao. 1996. Ca^{2+} transients associated with openings of inositol trisphosphate-gated channels in *Xenopus* oocytes. *J. Physiol. (Lond.).* 491:663–668.

Parker, I., W. J. Zang, and W. G. Wier. 1996. Ca^{2+} sparks involving multiple Ca^{2+} release sites along Z-lines in rat heart cells. *J. Physiol. (Lond.).* 497:31–38.

Post, J. A., and G. A. Langer. 1992. Sarcolemmal calcium binding sites in heart. I. Molecular origin in "gas-dissected" sarcolemma. *J. Membr. Biol.* 129:49–57.

Pratusevich, V. R., and C. W. Balke. 1996. Factors shaping the confocal image of the calcium spark in cardiac muscle cells. *Biophys. J.* 71: 2942–2957.

Roberts, W. M. 1993. Spatial Ca^{2+} buffering in saccular hair cells. *Nature.* 363:74–76.

Satoh, H., L. A. Blatter, and D. M. Bers. 1997. Effects of $[Ca^{2+}]_i$, SR Ca^{2+} load, and rest on Ca^{2+} spark frequency in ventricular myocytes. *Am. J. Physiol.* 272:H657–H668.

Shacklock, P. S., W. G. Wier, and C. W. Balke. 1995. Local Ca^{2+} transients (Ca^{2+}-sparks) originate at transverse tubules in rat heart cells. *J. Physiol. (Lond.).* 487:601–608.

Sham, J. S. 1997. Ca^{2+} release-induced inactivation of Ca^{2+} current in rat ventricular myocytes: evidence for local Ca^{2+} signaling. *J. Physiol. (Lond.).* 500:285–295.

Sipido, K. R., and W. G. Wier. 1991. Flux of Ca^{2+} across the sarcoplasmic reticulum of Guinea-pig cardiac cells during excitation-contraction coupling. *J. Physiol. (Lond.).* 435:605–630.

Smith, G. D. 1985. Numerical Solution of Partial Differential Equations: Finite Difference Methods. Oxford Applied Mathematics and Computing Science Series, 3rd ed. Clarendon Press, Oxford, UK. 75–76.

Smith, G. D. 1996. Analytical steady-state solution to the rapid buffering approximation near an open Ca^{2+} channel. *Biophys. J.* 71:3064–3072.

Smith, G., J. Wagner, and J. Keizer. 1996. Validity of the rapid buffering approximation near a point source of Ca^{2+} ions. *Biophys. J.* 70: 2527–2539.

Soeller, C., and M. B. Cannell. 1997. Numerical simulation of local calcium movements during L-type calcium channel gating in the cardiac diad. *Biophys. J.* 73:97–111.

Song, L.-S., M. D. Stern, E. G. Lakatta, and H. Cheng. 1997. Partial depletion of sarcoplasmic reticulum calcium does not prevent calcium sparks in rat ventricular myocytes. *J. Physiol. (Lond.).* 505:655–675.

Stern, M. D. 1992a. Buffering of Ca^{2+} in the vicinity of a channel pore. *Cell Calcium.* 13:183–192.

Stern, M. D. 1992b. Theory of excitation-contraction coupling in cardiac muscle. *Biophys. J.* 63:497–517.

Sun, X.-H., F. Protasi, M. Takahashi, H. Takeshima, D. G. Ferguson, and C. Franzini-Armstrong. 1995. Molecular architecture of membranes involved in excitation-contraction coupling of cardiac muscle. *J. Cell Biol.* 129:659–671.

Tinker, A., A. R. G. Lindsay, and A. J. Williams. 1993. Cation conductance in the calcium release channel of the cardiac sarcoplasmic reticulum under physiological and pathophysiological conditions. *Cardiovasc. Res.* 27:1820–1825.

Tsugorka, A., E. Riós, and L. A. Blatter. 1995. Imaging elementary events of calcium release in skeletal muscle cells. *Nature.* 269:1723–1726.

Wagner, J., and J. Keizer. 1994. Effects of rapid buffers on Ca^{2+} diffusion and Ca^{2+} oscillations. *Biophys. J.* 67:447–456.

Wang, J. H. 1953. Tracer-diffusion in liquid. IV. Self-diffusion of calcium ion and chloride ion in aqueous calcium chloride solutions. *J. Am. Chem. Soc.* 75:1769–1770.

Wang, W., Y. J. Suzuki, L. Cleemann, L. R. Jones, and M. Morad. 1997. Ca^{2+} sparks and Ca^{2+} release in transgenic myocytes overexpressing cardiac calsequestrin. *Biophys. J.* 72:44*a* (Abstr.).

Xiao, R.-P., H. H. Valdivia, K. Bogdanov, C. Valdivia, E. G. Lakatta, and H. Cheng. 1997. The immunophilin FK506 binding protein (FKBP) modulates Ca^{2+} release channel closure in rat heart. *J. Physiol. (Lond.).* 500:331–342.

Yao, Y., J. Choi, and I. Parker. 1995. Quantal puffs of intracellular Ca^{2+} evoked by IP_3 in *Xenopus* oocytes. *J. Physiol. (Lond.).* 491:663–668.